Acta Geochim
https://doi.org/10.1007/s11631-024-00708-z

ORIGINAL ARTICLE

Petrogenesis of late Cretaceous high Ba–Sr granodiorites, SE Lhasa block, China: implications for the reworking of juvenile crust and continental growth

Li-Hang Lin[1] · Ren-Zhi Zhu[1] · Shao-Cong Lai[1] · Jiang-Feng Qin[1] · Yu Zhu[1] · Shao-Wei Zhao[2] · Min Liu[1]

Received: 10 January 2024 / Revised: 15 May 2024 / Accepted: 23 May 2024

Abstract The high Ba–Sr rocks can provide significant clues about the evolution of the continent lithosphere, but their petrogenesis remains controversial. Identifying the Late Cretaceous high Ba–Sr granodiorites in the SE Lhasa Block could potentially provide valuable insights into the continent evolution of the Qinghai-Tibet Plateau. Zircon U–Pb ages suggest that the granodiorites were emplaced at 87.32 ± 0.43 Ma. Geochemically, the high Ba–Sr granodiorites are characterized by elevated $K_2O + Na_2O$ contents (8.18–8.73 wt%) and K_2O/Na_2O ratios (0.99–1.25, mostly > 1), and belong to high-K calc-alkaline to shoshonitic series. The Yonglaga granodiorites show notably high Sr (653–783 ppm) and Ba (1346–1531 ppm) contents, plus high Sr/Y (30.92–38.18) and $(La/Yb)_N$ (27.7–34.7) ratios, but low Y (20.0–22.8 ppm) and Yb (1.92–2.19 ppm) contents with absence of negative Eu anomalies (δEu = 0.83–0.88), all similar to typical high Ba–Sr granitoids. The variable zircon $\varepsilon Hf(t)$ values of − 4.58 to + 12.97, elevated initial $^{87}Sr/^{86}Sr$ isotopic ratios of 0.707254 to 0.707322 and low $\varepsilon Nd(t)$ values of − 2.8 to − 3.6 with decoupling from the Hf system suggest that a metasomatized mantle source included significant recycled ancient materials. The occurrence of such high Ba–Sr intrusions indicates previous contributions of metasomatized mantle-derived juvenile material to the continents, which imply the growth of continental crust during the Late Cretaceous in the SE Lhasa. Together with regional data, we infer that the underplated mafic magma provides a significant amount of heat, which leads to partial melting of the juvenile crust. The melting of the metasomatized mantle could produce a juvenile mafic lower crust, from which the high Ba–Sr granitoids were derived from reworking of previous mafic crust during the Late Cretaceous (ca. 100–80 Ma) in the SE Lhasa.

Keywords Late Cretaceous · High Ba–Sr granodiorites · SE Lhasa · Growth of continental crust · Juvenile crust

1 Introduction

The Qinghai-Tibet Plateau has played a significant role in recent Earth evolution and climate change, but the complicated geological processes of the Qinghai-Tibet Plateau are still hotly debated in recent years (Ma et al. 2022; Zhang et al. 2017). There is a consensus that the origin of the Qinghai-Tibet Plateau can be attributed to the collision between India and Asia during the Late Cenozoic period (Haider et al. 2013; Hetzel et al. 2011; Liu et al. 2014; Zhang et al. 2004), following Mesozoic continental accretion, subduction, and crustal thickening (Decelles et al. 2007; Murphy et al. 1997).

The Lhasa terrane (LT) represents the final continental fragment integrated into the plateau during the Late Mesozoic era (Chen et al. 2015; Yin and Harrison 2000; Zhu et al. 2011) and has gone through noteworthy S–N crustal thickening and shortening during the Late Cretaceous before the collision between India and Asia (Decelles et al. 2007; Kapp et al. 2007; Murphy et al. 1997; Pan et al. 2014; Yin

Supplementary Information The online version contains supplementary material available at https://doi.org/10.1007/s11631-024-00708-z.

✉ Ren-Zhi Zhu
renzhi@nwu.edu.cn

[1] State Key Laboratory of Continental Dynamics, Department of Geology, Northwest University, Xi'an 710069, China

[2] Ministry of Education Key Laboratory of Western China's Mineral Resources and Geological Engineering, School of Earth Science and Resources, Chang'an University, Xi'an 710054, China

Published online: 23 June 2024

and Harrison 2000). Responding to tectonic processes, Late Cretaceous magmatism occurred in the LT and has been thought to be related to either the subduction of the Neo-Tethyan Ocean lithosphere or to crustal thickening (Chen et al. 2015; Ma and Yue 2010; Pan et al. 2014). Recently, the Late Cretaceous (~ 80 Ma) felsic magmatism reported in the LT is thought to be related to the subducted Neo-Tethys oceanic slab (Chapman et al. 2018; Wang et al. 2019, 2021). Some workers have argued that the Late Cretaceous (~ 90 Ma) adakitic, Mg-rich, and K-rich rocks in the LT resulted from the lithospheric delamination underneath the thickened crust after the collision of Lhasa-Qiangtang Blocks (Chen et al. 2015; Ji et al. 2021; Li et al. 2013; Liu et al. 2017; Sun et al. 2015a, b, 2020; Wang et al. 2014; Yi et al. 2018; Zhao et al. 2008), but this explanation has been challenged based on evidence from zircon xenocrysts in Lhasa ultrapotassic magmas (Liu et al. 2014). It is noteworthy that the majority of Late Cretaceous magmatism in central Lhasa terrane (CLT), northern Lhasa terrane (NLT), and southern Qiangtang terrane (SQT) has been attributed to the reworking of juvenile crust through partial melting of pre-existing underplated lower crust (Wang et al. 2021; Tang et al. 2019). Moreover, the role of mantle-derived magmas and whether crustal reworking or growth occurred in the SE Lhasa during the Late Cretaceous period (ca. 100–80 Ma) are poorly known. Therefore, Late Cretaceous potassium-rich high Ba–Sr granodiorites may offer valuable insights into magmatic evolution associated with mantle-derived materials. In this paper, our studies provide bulk-rock chemical, isotopic and in situ zircon Hf isotopic and U–Pb age data to constrain: (1) the petrogenesis of high Ba–Sr granodiorites; and (2) the possible geodynamic processes at depth after final Lhasa-Qiangtang amalgamation in the Qinghai-Tibet Plateau.

2 Geological setting and petrography

The Qinghai-Tibet Plateau constitutes a significant component of the Tethyan-related orogenic collage of the predominantly EW trending Himalaya, Qiangtang, Lhasa, Songpan-Ganzi, and Kunlun-Qiadam terranes. These terranes are demarcated by the Yarlung-Zangbo (YZ), Bangong-Nujiang (BN), Kunlun, and Jinsha suture zone (Fig. 1a) (Yin and Harrison 2000).

The LT lies between the BN suture to the northern and the YZ suture to the southern (Fig. 1a) (Chiu et al. 2009). Its detachment from Gondwana occurred during the Permian to Triassic period, succeeded by a northward movement and eventual convergence with the Qiangtang terrane (QT) during the Late Jurassic period to Early Cretaceous period (Kapp et al. 2005, 2007; Zhu et al. 2011). The LT has been shown to contain three distinct magmatic belts (Fig. 1b) (Chiu et al. 2009): extensive Linzizong volcanic successions and Gangdese batholiths, spanning from the Cretaceous to the Early Tertiary, are widely distributed in the southern Lhasa terrane (Harris et al. 1990; Ji et al. 2009a; Lee et al. 2009; Mo et al. 2007; Wang et al. 2022a, b; Wen et al. 2008a, b), and are considered to be the result of northward subduction of Neo-Tethyan oceanic lithosphere. There are also plentiful Mesozoic igneous rocks in the sub-terranes of NLT and CLT (Chiu et al. 2009; Chu et al. 2006; Guynn et al. 2006; Harris et al. 1990; Xu et al. 1985; Zhu et al. 2009a), the former associated with closure of the Bangong-Nujiang Tethyan ocean has been associated with the northern magmatic belt (Chen et al. 2014; Chiu et al. 2009; Hu et al. 2022; Qu et al. 2012; Sui et al. 2013; Zhu et al. 2009a, b, 2011, 2013, 2015). About the development of the Meso-Tethys, it is commonly believed that the Meso-Tethys oceanic plate underwent northward subduction beneath the QT margin located in the south (Li et al. 2013, 2016; Liu et al. 2017; Ji et al. 2021; Zhang et al. 2017). The collision between the QT and the LT during the Late Cretaceous followed the closure of Meso-Tethys and resulted in the thickening of the southern margin of the QT and the northern margin of the LT. The subsequent delamination of thickened lithosphere triggered a series of post-collisional magmatic events (Chen et al. 2015; Li et al. 2013; Ma et al. 2010; Meng et al. 2014; Qu et al. 2006; Sun et al. 2015a, b, 2020; Wang et al. 2014; Yi et al. 2018; Yu et al. 2011; Liu et al. 2017).

In SE Lhasa, a wide range of Cretaceous granitoids crop out in a NW–SE belt SW trending of the BN suture zone (Chiu et al. 2009; Pan et al. 2004; Zhu et al. 2009b), enclosed by the metamorphic rocks of Proterozoic, Devonian, and Carboniferous-Permian periods. These granitoids are predominantly found as batholiths, primarily distributed in the Bomi and Chayu regions (commonly referred to as Bomi-Chayu batholiths) (Chiu et al. 2009; Lin et al. 2013). They mainly comprise monzogranites and granodiorites, with minor occurrences of mafic enclaves and dioritic veins (Pan et al. 2004; Zhu et al. 2009b). This study focuses on the Yonglaga granitoid (Fig. 1c), located in the east of Gongshan County. It has a rounded, elongated shape aligned with the SE section of the Bomi-Chayu batholiths, positioned between the BN suture and the Jiali fault (Fig. 1b, c) (Chiu et al. 2009; Zhu et al. 2009b).

As is typical in the SE Lhasa Block, the granodiorites are poorly exposed. They are emplaced into Paleozoic (mainly Carboniferous) metasedimentary rocks, are undeformed and their margins are sharp but rarely chilled. High-Mg basaltic diorites are closely associated in the western margin of the granodiorites, also with sharp contacts, and both facies are elongated along the structural fabric of the surrounding metasediments (Fig. 1c). The Yonglaga high Ba–Sr granodiorites are fine-grained and mainly composed of quartz 12%–15%, alkali feldspar 28%–33%, sodic plagioclase

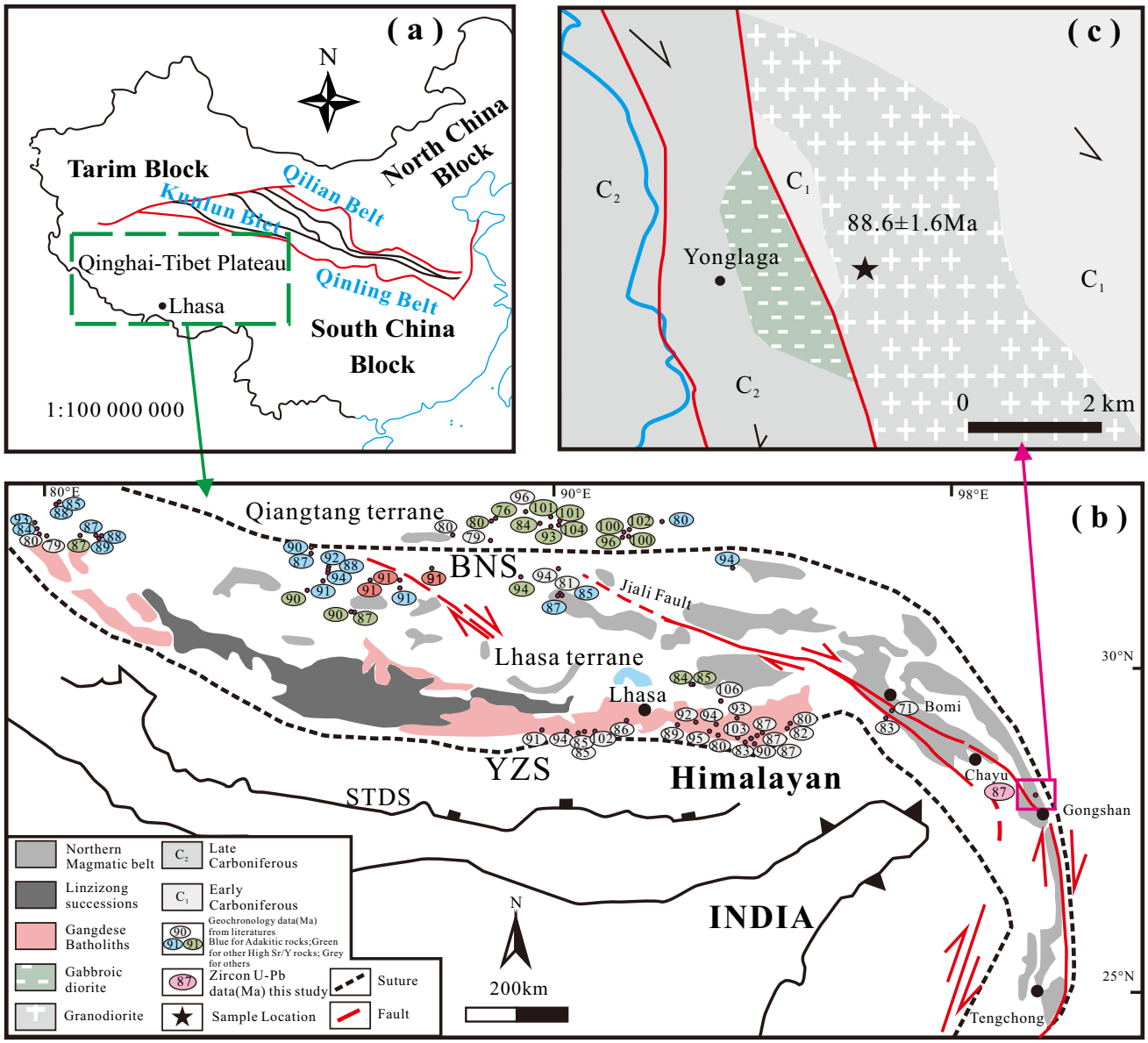

Fig. 1 **a** Simplified tectonic map of China. **b** Map of southern Qinghai-Tibet Plateau showing sample locations and major magmatic features (from Chiu et al. 2009). **c** Regional geology of Yonglaga (from Wang et al. 2021). The geochronology data are summarised in Table 5

40%–45%, hornblende ~ 5% and biotite ~ 5%, with accessory minerals such as zircon, apatite, titanite, magnetite, and other Ti–Fe oxides (Fig. 2).

3 Analytical methods

Bulk-rock samples were trimmed to remove weathered surfaces and cleaned with deionized water. They were then crushed and powdered through a 200 mesh screen using a tungsten carbide ball mill. Major elements were analyzed by X-ray fluorescence (XRF) spectrometry (Rikagu RIX 2100) at the Guizhou Tuopu Resource and Environmental Analysis Center, Institute of Geochemistry, Chinese Academy of Sciences in Guiyang, China. Analyses of USGS and Chinese national rock standards (GSP-2, BCR-2, and AGV-2) reveal analytical precision and accuracy for major elements typically better than 5%. Trace elements were determined by inductively coupled plasma mass spectrometry (ICP-MS) at the Guizhou Tuopu Resource and Environmental Analysis Center, Institute of Geochemistry, Chinese Academy of Sciences in Guiyang, China. A Bruker Aurora M90 ICP-MS was used, following the methodology described by Qi et al. (2000). Powders were dissolved in a high-pressure PTFE bomb using an HNO_3 + HF mixture at 185 °C for 36 h. The

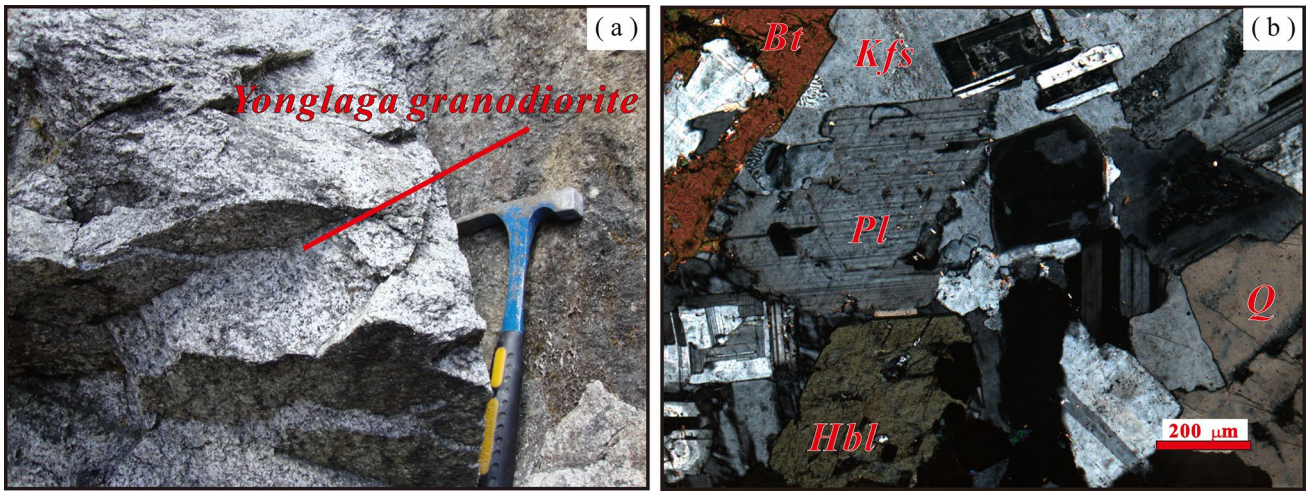

Fig. 2 Field photographs and photomicrographs of the Yonglaga high Ba–Sr granodiorites in the SE Lhasa Block, China

ICP-MS analyses have a relative accuracy and precision of approximately ± 5% to ± 10% for the majority of elements.

Bulk-rock Sr–Nd isotope measurements were conducted at the State Key Laboratory of Continental Dynamics, Northwest University, Xi'an, China, using a Nu Plasma HR multi-collector mass spectrometer, following a methodology similar to that described in Chu et al. (2009). Sr and Nd isotopic fractionation was adjusted to $^{87}Sr/^{86}Sr = 0.1194$ and $^{146}Nd/^{144}Nd = 0.7219$, respectively. JMC-Nd and NIST SRM-987 were used as certified reference standard solutions for the ratios of $^{143}Nd/^{144}Nd$ and $^{87}Sr/^{86}Sr$, respectively. AGV-2, GSP-2, and BHVO-2 were utilized as the reference materials.

The Yonglaga pluton was the source of two ~ 5 kg samples at different sampling locations, from which zircons were extracted separately. The separation of zircon grains was achieved using conventional techniques involving heavy liquid and magnetic methods. Selected zircon grains were manually chosen and mounted on epoxy resin discs, followed by polishing carbon coating. The internal structure was assessed using cathodoluminescence (CL) before conducting U–Pb analyses. Zircon U–Pb analyses used laser ablation ICP-MS with an Agilent 7500a ICP-MS instrument and a 193-nm laser at the State Key Laboratory of Continental Dynamics, Northwest University in Xi'an, China. The analytical method was based on the approach of Yuan et al. (2004). The GLITTER program was used to determine the ratios of $^{206}Pb/^{238}U$ and $^{207}Pb/^{206}Pb$, which were subsequently adjusted for accuracy using the Harvard zircon 91500 as an external calibration standard. These adjustment factors were subsequently utilized to rectify any potential discrepancies caused by instrumental mass bias and variations in elemental and isotopic distribution at different depths. The method described in Andersen (2002) was applied to assess the common Pb contents. ISOPLOT (version 3.0) (Ludwig 2003) was employed for age calculations and plotting of Concordia diagrams. The errors provided in tables and figures correspond to a confidence level of 2σ.

In situ zircon Hf isotopic analyses used a Neptune MC-ICP-MS with a 193-nm laser. The laser operated at a repetition rate of 10 Hz and an energy level of 100 MJ, while the spot sizes were maintained at 32 μm. The detailed analytical technique follows Yuan et al. (2008). During the analysis, the $^{176}Hf/^{177}Hf$ and $^{176}Lu/^{177}Hf$ ratios of the standard zircon (91500) were found to be approximately 0.282294 ± 15 (2σ, n = 20) and 0.00031 respectively, which are similar to the widely accepted values of 0.282302 ± 8 and 0.282306 ± 8 (2σ) obtained using the solution method (Goolaerts et al. 2004). The definitions of $\varepsilon Hf(t)$ value, $f_{Lu/Hf}$ ratio, single-stage model age (T_{DM1}), and two-stage model age (T_{DM2}) are provided with reference to Zheng et al. (2008).

4 Results

Major and trace element results can be found in Table 1, the whole-rock Sr–Nd isotopic results are listed in Table 2, and zircon Hf isotopes are presented in Table 3. The zircon U–Pb ages can be accessed from the Supplementary Dataset Table.

4.1 Zircon U–Pb age

Relevant zircons are examined in the Gongshan region in SE Lhasa (Fig. 3a). Detailed information on sampling locations, lithology, and dating outcomes can be found in Figs. 1, 2, and 3 as well as the Supplementary Dataset Table.

Zircon grains from the Yonglaga granodiorite (YLG15-1) are euhedral, prismatic, and mostly have

Table 1 The major (wt%) and trace element (ppm) results of rocks from Yonglaga pluton

Sample	High Ba–Sr granodiorites								
	YLG15-1	YLG15-2	YLG15-3	YLG15-4	YLG15-5	YLG15-6	YLG15-7	YLG15-11	YLG15-12
SiO_2	63.74	63.96	64.24	63.30	63.17	64.56	64.19	64.55	64.28
TiO_2	0.45	0.44	0.43	0.45	0.48	0.44	0.48	0.45	0.45
Al_2O_3	16.43	16.32	16.41	16.59	16.47	16.37	16.47	16.23	16.13
Fe_2O_3T	4.33	4.29	4.19	4.41	4.53	4.19	4.42	4.12	4.19
MnO	0.07	0.07	0.07	0.07	0.07	0.07	0.07	0.06	0.06
MgO	1.49	1.48	1.43	1.51	1.54	1.45	1.55	1.48	1.49
CaO	3.25	3.17	3.03	3.20	3.30	3.06	3.22	3.08	3.13
Na_2O	4.07	4.16	3.85	4.29	4.20	3.93	3.99	4.08	4.13
K_2O	4.49	4.45	4.80	4.40	4.53	4.79	4.44	4.10	4.10
P_2O_5	0.41	0.39	0.39	0.37	0.37	0.39	0.36	0.34	0.34
LOI	1.09	1.15	1.13	0.97	0.85	1.00	1.10	1.47	1.70
TOTAL	99.82	99.88	99.97	99.56	99.51	100.25	100.29	99.96	100.00
Li	28.6	27.8	27.1	20.8	23.0	26.5	22.6	26.1	27.1
Be	3.56	3.73	3.35	3.43	3.39	3.26	3.37	3.44	3.54
Sc	5.34	5.44	5.27	5.53	6.10	5.26	5.89	5.58	5.63
V	56.5	57.4	54.1	52.8	54.5	54.6	53.9	49.8	51.8
Cr	7.65	7.89	7.30	10.0	11.8	7.15	11.4	14.6	11.9
Co	15.5	14.6	26.0	16.1	24.5	19.6	23.4	18.3	20.2
Ni	5.69	5.72	5.77	6.25	6.42	5.46	6.32	8.50	6.99
Cu	4.18	4.24	4.39	3.53	3.15	4.46	3.26	2.57	2.63
Zn	40.4	42.0	40.0	39.8	37.9	39.7	38.6	31.7	32.3
Ga	18.9	19.5	18.7	18.5	18.6	18.6	18.6	18.2	18.4
Ge	1.40	1.35	1.40	1.35	1.43	1.40	1.40	1.39	1.39
Rb	179	184	182	170	175	182	176	167	170
Sr	754	783	748	709	712	750	721	653	658
Y	20.5	20.5	20.0	20.1	22.8	20.3	21.2	21.1	21.1
Zr	241	244	254	243	268	241	265	243	242
Nb	14.2	14.0	14.0	12.0	14.3	14.2	13.1	14.1	13.9
Cs	4.86	4.98	4.90	4.43	4.61	4.89	4.69	4.36	4.46
Ba	1413	1448	1525	1347	1373	1518	1381	1348	1346
La	96.9	84.2	85.5	80.7	92.5	82.3	80.4	74.7	77.7
Ce	169	150	152	144	165	147	145	136	140
Pr	16.8	14.8	15.1	14.3	16.8	14.7	14.8	13.8	14.0
Nd	54.4	50.8	51.0	49.2	55.6	49.7	50.4	48.6	48.7
Sm	7.54	7.25	7.25	7.07	8.03	7.09	7.31	7.23	7.15
Eu	1.82	1.80	1.74	1.77	1.94	1.74	1.84	1.74	1.75
Gd	5.86	5.62	5.57	5.49	6.20	5.46	5.67	5.55	5.52
Tb	0.72	0.70	0.69	0.68	0.77	0.68	0.71	0.71	0.70
Dy	3.64	3.59	3.52	3.53	4.04	3.55	3.75	3.72	3.65
Ho	0.69	0.69	0.66	0.67	0.76	0.67	0.71	0.70	0.70
Er	2.03	1.99	1.94	1.94	2.19	1.93	2.04	2.04	1.99
Tm	0.30	0.30	0.29	0.29	0.33	0.29	0.30	0.31	0.30
Yb	2.01	2.00	1.97	1.92	2.17	1.93	2.03	2.02	2.02
Lu	0.32	0.31	0.31	0.30	0.34	0.30	0.32	0.32	0.31
Hf	5.70	5.73	5.94	5.54	6.06	5.54	5.91	5.46	5.47
Ta	1.07	1.04	1.09	0.81	1.05	1.11	0.93	1.06	1.04
Pb	19.5	20.7	21.0	18.1	18.1	20.5	19.2	18.6	18.9
Th	38.3	41.3	40.4	31.2	34.7	35.2	35.3	30.8	32.5

Table 1 (continued)

Sample	High Ba–Sr granodiorites								
	YLG15-1	YLG15-2	YLG15-3	YLG15-4	YLG15-5	YLG15-6	YLG15-7	YLG15-11	YLG15-12
U	5.60	7.11	6.26	5.44	5.58	5.64	5.95	5.70	6.12
Mg#	44.5	44.6	44.3	44.4	44.2	44.6	45.0	45.6	45.3
A/CNK	0.94	0.94	0.96	0.94	0.92	0.95	0.96	0.97	0.95
Sr/Y	36.7	38.2	37.4	35.2	31.2	36.9	34.1	30.9	31.2
T_{Zr}(℃)	794	795	803	793	799	796	805	800	798

Table 2 The whole-rock Rb–Sr and Sm–Nd isotopic data for rocks from Yonglaga pluton

Sample	$^{87}Sr/^{86}Sr$	2SE	Sr(ppm)	Rb(ppm)	$^{143}Nd/^{144}Nd$	$2s_m$	Nd(ppm)	Sm(ppm)	Model Age (Ga)	$\varepsilon_{Nd}(t)$	I_{Sr}
YLG15-1	0.708140	0.000006	754	179	0.512429	0.000003	54.4	7.5	0.96	−2.8	0.707293
YLG15-2	0.708162	0.000005	783	184	0.512398	0.000004	50.8	7.3	1.01	−3.5	0.707322
YLG15-3	0.708124	0.000007	748	182	0.512388	0.000007	51.0	7.2	1.02	−3.6	0.707254

$^{87}Rb/^{86}Sr$ and $^{147}Sm/^{144}Nd$ ratios were calculated using Rb, Sr, Sm and Nd contents analyzed by ICP-MS

T_{2DM} represent the two-stage model age and were calculated using present-day $(^{147}Sm/^{144}Nd)_{DM}=0.2137$, $(^{147}Sm/^{144}Nd)_{DM}=0.51315$ and $(^{147}Sm/^{144}Nd)crust=0.1012$. $\varepsilon_{Nd}(t)$ values were calculated using present-day $(^{147}Sm/^{144}Nd)_{CHUR}=0.1967$ and $(^{147}Sm/^{144}Nd)_{CHUR}=0.512638$. $\varepsilon_{Nd}(t)=[(^{143}Nd/^{144}Nd)_{sample}(t)/(^{143}Nd/^{144}Nd)_{CHUR}(t)\text{-}1]\times10^4$, $T_{2DM}=1/\lambda\times\{1+[(^{143}Nd/^{144}Nd)sample\text{-}((^{147}Sm/^{144}Nd)sample\text{-}(^{147}Sm/^{144}Nd)crust)\times(e^{\lambda t}\text{-}1)\text{-}(^{143}Nd/^{144}Nd)_{DM}]/((^{147}Sm/^{144}Nd)_{crust}\text{-}(^{147}Sm/^{144}Nd)_{DM})\}$

clear oscillatory zones (Fig. 3a), typical of magmatic zircons. The twenty-eight reliable analyses show high Th (435–2382 ppm) and U (538–1361 ppm) with Th/U ratios of 0.61–1.80. The data form a coherent group yielding $^{206}Pb/^{238}U$ ages from 85.2 ± 0.8 to 89.4 ± 1.0 Ma, with a weighted mean age of 87.32 ± 0.43 Ma (MSWD = 1.7, $n = 28$, 2σ), taken to indicate the crystallization age (Fig. 3b).

4.2 Major and trace element geochemistry

The granodiorites have comparatively uniform SiO_2 (63.17wt%–64.56wt%), with high Na_2O (3.85wt%–4.29wt%) and K_2O contents (4.10wt%–4.82wt%) (Fig. 4a, b). They plot within the domains of high Ba–Sr granites and high Sr/Y and adakitic rocks in the CLT, NLT and SQT, and show a shoshonitic affinity which is similar to the typical high Ba–Sr rocks (Fig. 4a, b). They also have low TiO_2, CaO, Fe_2O_3T, MnO, P_2O_5, and MgO with $Mg^{\#}$ of 44.2–45.6 (Fig. 4c and 7), but exhibit moderate Al_2O_3 contents of 16.13–16.59 wt% with A/CNK (molar $Al_2O_3/CaO+Na_2O+K_2O$) ratios of 0.92–0.97 (Fig. 4d). Figure 5a shows positive anomalies for Rb, U, Th, Pb, and Nd, and depletions in P, Ti, Nb, and Ta. Figure 5b shows high total REE contents (297–362 ppm) and fractionated LREE/HREE with high $(La/Yb)_N$ (27.7–34.7) and small negative Eu anomalies (δEu = 0.83–0.88). Both the major and trace elements share similar characteristics with the typical high Ba–Sr granites and Late Cretaceous adakites plus high Sr/Y rocks in the CLT, NLT, and SQT (Fig. 5, 6 and 7).

4.3 Whole-rock Sr–Nd and zircon Hf isotopes

Whole-rock Sr–Nd isotope results are listed in Table 2. All $\varepsilon Nd(t)$ values and initial $^{87}Sr/^{86}Sr$ isotopic ratios (I_{Sr}) are computed for the crystallization age and are very similar. The high Ba–Sr granodiorites (sample YLG15-1, -2, and -3) have I_{Sr} ratios ranging from 0.707254 to 0.707322 and $\varepsilon Nd(t)$ values ranging from –2.8 to –3.6, with T_{DM} values of 0.96–1.02 Ga (Fig. 8b).

Zircons Lu–Hf data are presented in Table 3 and Fig. 8a, with initial $^{176}Hf/^{177}Hf$ ratios and $\varepsilon Hf(t)$ values based on crystallization age. The zircons display a range of Hf isotopic compositions, from −4.55 to + 13.01 (24 zircons, including two negative ones), and Hf model ages of 319–1440 Ma. These contrast markedly from the Nd data described above, signifying a clear decoupling of Hf and Nd isotope systems (Fig. 8c).

5 Discussion

5.1 Petrogenesis of the Yonglaga high Ba–Sr granodiorites

The Yonglaga granodiorites analyzed in this study have high alkali contents (Na_2O+K_2O = 8.18wt%–8.73wt%, Table 1) and LREEs (282–347 ppm), Sr (653–783 ppm),

Table 3 Single-grain zircon Hf isotopic data for Yonglaga pluton

Grain spot	Age (Ma)	$^{176}Yb/^{177}Hf$	2SE	$^{176}Lu/^{177}Hf$	2SE	$^{176}Hf/^{177}Hf$	2SE	$(^{176}Hf/^{177}Hf)_i$	$\varepsilon_{Hf}(0)$	$\varepsilon_{Hf}(t)$	2SE	T_{DM1}(Ma)	T_{DM2}(Ma)	$f_{Lu/Hf}$
High Ba–Sr granodiorites (YLG15-1)														
Spot-01	87.1	0.061914	0.000941	0.002038	0.000027	0.282739	0.000030	0.282736	–1.17	0.62	1.07	748	1110	−0.94
Spot-02	86.1	0.037262	0.000295	0.001098	0.000006	0.282862	0.000016	0.282860	3.18	5.01	0.56	555	830	−0.97
Spot-03	87.3	0.034416	0.000229	0.001007	0.000006	0.282846	0.000014	0.282844	2.62	4.47	0.49	576	865	−0.97
Spot-04	88.8	0.096803	0.000676	0.002907	0.000040	0.283062	0.000021	0.283057	10.26	12.04	0.74	283	382	−0.91
Spot-05	86.5	0.044594	0.000360	0.001278	0.000011	0.282846	0.000015	0.282844	2.61	4.43	0.54	581	867	−0.96
Spot-06	86.9	0.042161	0.000182	0.001456	0.000006	0.282754	0.000044	0.282751	–0.64	1.18	1.55	715	1075	−0.96
Spot-07	87.7	0.069243	0.000942	0.002277	0.000023	0.282956	0.000041	0.282953	6.52	8.31	1.44	434	620	−0.93
Spot-08	89.4	0.030719	0.000086	0.000940	0.000002	0.282790	0.000012	0.282788	0.62	2.52	0.43	655	991	−0.97
Spot-09	88.1	0.033577	0.000390	0.001040	0.000012	0.282850	0.000018	0.282848	2.75	4.62	0.65	571	856	−0.97
Spot-10	86.9	0.058764	0.000807	0.001602	0.000020	0.282939	0.000014	0.282936	5.89	7.70	0.50	452	658	−0.95
Spot-11	88	0.043093	0.000332	0.001282	0.000015	0.282835	0.000016	0.282833	2.24	4.09	0.56	596	890	−0.96
Spot-12	88.4	0.064055	0.001368	0.002020	0.000041	0.282922	0.000033	0.282919	5.32	7.14	1.18	481	696	−0.94
Spot-13	88.1	0.067235	0.000327	0.002210	0.000003	0.282716	0.000035	0.282712	–2.00	-0.19	1.23	786	1163	−0.93
Spot-14	86.8	0.044076	0.000208	0.001542	0.000006	0.282975	0.000026	0.282973	7.19	9.00	0.94	398	575	−0.95
Spot-15	89.3	0.045672	0.000160	0.001485	0.000005	0.282591	0.000177	0.282588	-6.41	-4.55	6.24	949	1440	−0.96
Spot-16	86.4	0.057072	0.000158	0.001659	0.000003	0.282872	0.000012	0.282870	3.55	5.35	0.44	548	809	−0.95
Spot-17	88.9	0.028319	0.000273	0.000817	0.000007	0.282809	0.000013	0.282808	1.31	3.21	0.46	626	947	−0.98
Spot-18	86.1	0.048549	0.000093	0.001437	0.000008	0.282935	0.000019	0.282932	5.76	7.56	0.69	455	667	−0.96
Spot-19	88	0.038564	0.000241	0.001099	0.000004	0.282874	0.000015	0.282872	3.59	5.46	0.53	538	803	−0.97
Spot-20	86	0.050036	0.000290	0.001366	0.000007	0.282909	0.000013	0.282906	4.83	6.64	0.46	492	726	−0.96
Spot-21	87.3	0.042016	0.000419	0.001249	0.000012	0.282854	0.000017	0.282852	2.91	4.76	0.60	568	847	−0.96
Spot-22	87.8	0.036272	0.000162	0.001106	0.000005	0.282786	0.000014	0.282784	0.49	2.35	0.51	663	1001	−0.97
Spot-23	87.7	0.115607	0.000387	0.003203	0.000007	0.283091	0.000025	0.283085	11.27	13.01	0.89	242	319	−0.90
Spot-24	87.2	0.041339	0.000331	0.001212	0.000009	0.282803	0.000016	0.282801	1.11	2.95	0.58	640	962	−0.96

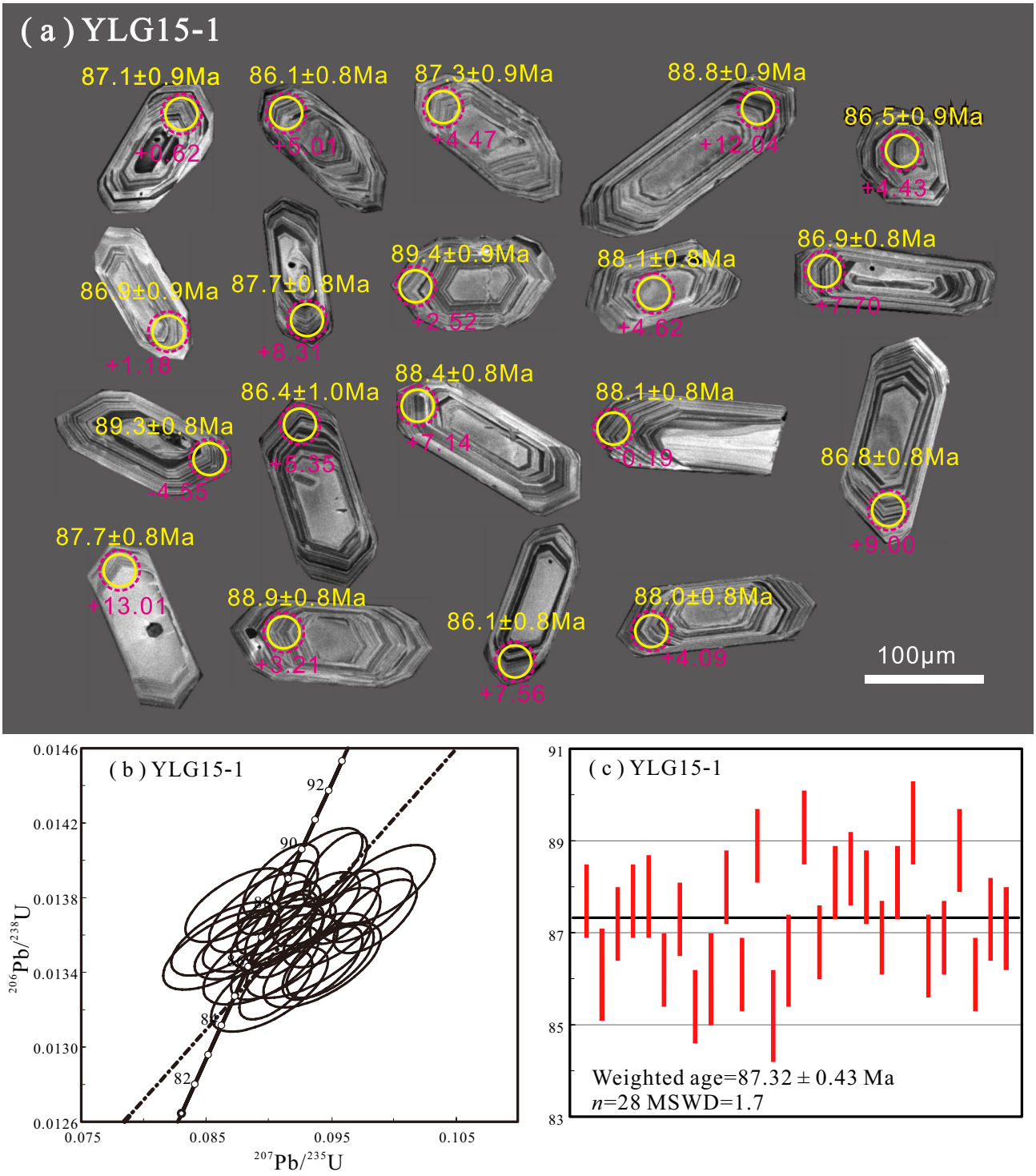

Fig. 3 **a** CL images of representative zircon grains from the high Ba–Sr Yonglaga granitoids, SE Tibet. **b** LA-ICP-MS zircon U–Pb concordia diagram of representative zircon grains from the high Ba–Sr Yonglaga granitoids, China

and Ba (1346–1531 ppm), low Nb, Ta and HREEs with an absence of negative Eu anomalies (δEu = 0.83–0.88) (Fig. 5), all of which suggest distinction from classical A-type, I-type, and S-type granites, but similarity with typical high Ba–Sr granitoids (Fowler and Henney 1996; Fowler et al. 2001, 2008; Jiang et al. 2006, 2012; Peng et al. 2013; Qian et al. 2002; Ye et al. 2008). Although they could be compared with adakites in many geochemical

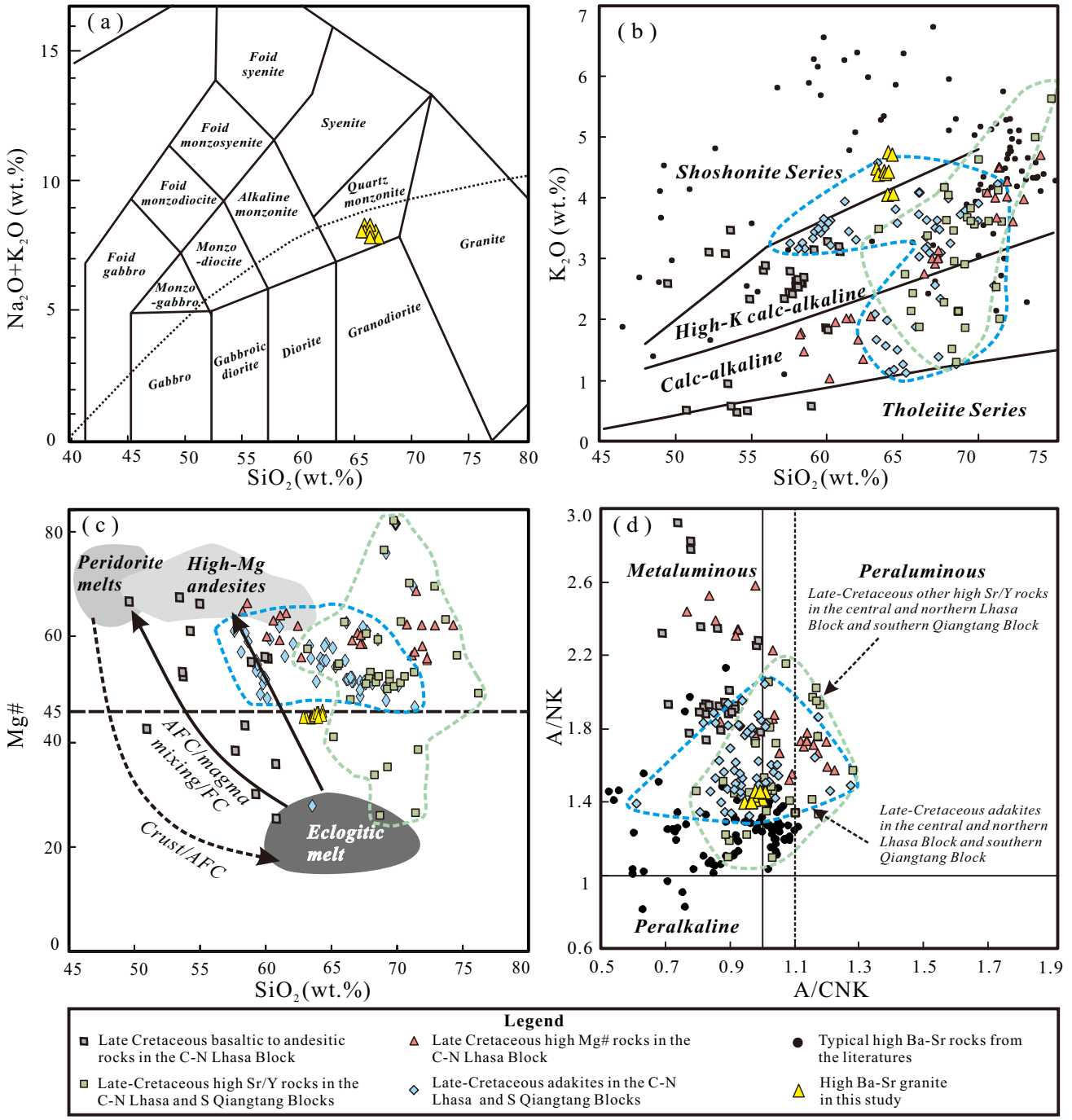

Fig. 4 **a** Na_2O+K_2O versus SiO_2 diagram; **b** K_2O vs SiO_2 diagram; **c** Mg# versus SiO_2 systematic diagram (from Moyen and Martin 2012); **d** A/NK versus A/CNK diagram for the high Ba–Sr Yonglaga granitoids in the SE Lhasa. Experimentally obtained compositions of partial melts by dehydration melting of different source rocks under crustal P–T conditions (0.5–1.5 GPa, 800–1000 °C, Patiño Douce and Beard 1995). The data of Late Cretaceous adakites and high Sr/Y rocks are summarized in Table 5

characteristics, such as the high Sr and LREEs, low HREEs, Nb, and Ta plus lack of negative Eu anomalies, there are some significant differences: (1) the notably higher alkali contents ($Na_2O+K_2O>8.2$) and higher K_2O/Na_2O ratios (0.99–1.25) than adakites ($K_2O/Na_2O<0.5$); (2) a shoshonitic affinity rather than the calc-alkaline trend of adakites (Fig. 4b); (3) the presence of coeval high-Mg basaltic rocks which do not show adakitic signature (Polat and Kerrich 2001; Zhu et al. 2024). Thus, the typical high Ba–Sr granite signature can still be recognized despite

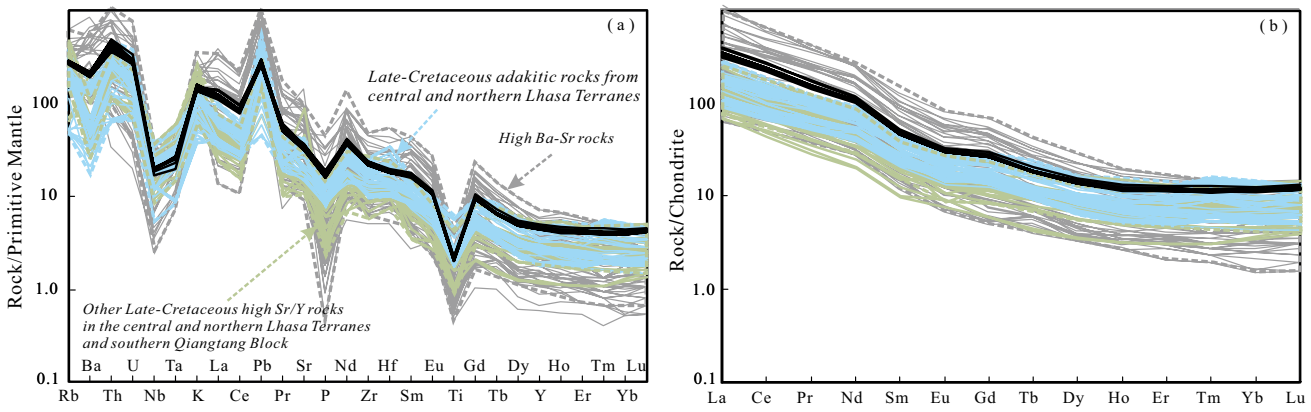

Fig. 5 Primitive-mantle-normalized trace element spider diagram and Chondrite-normalized REE patterns (**a**, **b**) for the high Ba–Sr Yonglaga granitoids in the SE Lhasa. The primitive mantle and chondrite values are from Sun and McDonough (1989)

clear overlap with adakitic rocks (Fig. 6a, b) (Tarney and Jones 1994; Ye et al. 2008).

5.1.1 The origin of high Ba–Sr granodiorites

Tarney and Jones (1994) initially suggested three genetic models for high Ba–Sr granites: (i) the lower veined lithospheric mantle is enriched by small amounts of carbonatitic melts from the asthenosphere through penetration; (ii) partial melting of the ocean plateaus or subducted ocean islands; (iii) hydrous partial melting of underplated mafic magmas. Other explanations have been proposed, including partial melting of thickened mafic lower crust with participation of minor LILE-rich appinitic magma (Table 4) (Ye et al. 2008); low degree partial melting of the sub-continental lithospheric mantle (Jiang et al. 2006) with subsequently metasomatized by minor crustal materials contamination (Fowler and Henney 1996; Fowler et al. 2001, 2008); continental slab-derived melts (Jiang et al. 2012), and subduction-related melts or fluids (Qian et al. 2002; Peng et al. 2013). Given this ongoing debate, it is important to determine whether the high Ba–Sr granodiorites are derived from the mantle or crust and investigate any interaction in between.

The presence of a mafic intrusion near the granitoid pluton area. The mafic xenolith and enclave were also not detected in the granodiorites, suggesting that a crust-mantle magma mixing model lacked geological evidence. Zhu et al. (2024) have reported the geochemical characteristics of the high-Mg basaltic rocks in the Yonglaga area. The age relationships and sharp contacts in the field between the high-Mg basaltic rocks and the granodiorites, and the notable compositional gap all suggest that the granodiorites are unlikely to have formed by simple crystal fractionation of these basaltic magmas (Fig. 7). Geochemically, the Yonglaga granodiorites display a weak correlation between SiO_2 and other major elements (Fig. 7), indicating a limited role for fractional crystallization during magma evolution. On the plots of La/Nb vs. La and Th/Nb vs. Th diagram (Fig. 6c, d), the Yonglaga granodiorites show clear linear trends, indicating that a partial melting process that plays a significant role in their formation rather than the fractional crystallization processes. Limited crustal contamination is suggested by the significantly higher Ba (1346–1525 ppm) and Sr (653–783 ppm) than the average Ba (390 ppm) and Sr (325 ppm) of the continental crust (Rudnick and Fountain 1995), plus Rb/Nb ratios that do not show any obvious correlation with SiO_2. The highest LOI (1.70 wt%) sample has lower Ba (1346 ppm) and Sr (658 ppm), suggesting a similarly limited role for alteration in defining the characteristic chemistry of the rocks.

The collision zone between LT and QT underwent a gentle collision and slab detachment of a slab during 140–110 Ma (Chen et al. 2014; Qu et al. 2012; Sui et al. 2013; Zhao et al. 2008; Zhu et al. 2009a, b, 2011, 2013, 2015), the non-marine facies of the BN suture have been present since approximately 118 Ma (Kapp et al. 2005, 2007), and the unaltered plutons that intrude ophiolitic mélanges of the BN suture have zircon U–Pb ages ranging from 116 to 112 Ma (Hu et al. 2022), indicating that the BNTO subduction-related activity would have been unlikely during generation and intrusion of the high Ba–Sr granodiorites. Therefore, the Yonglaga high Ba–Sr granodiorites are post-collisional shoshonitic granitoids during the Late Cretaceous, precluding a source related to the partial melting of subducted ocean islands or plateaus.

The Yonglaga granodiorites have low $Mg^{\#}$ (44.2–45.3) values, low Cr (7.65–14.6 ppm) and Ni (5.69–8.50 ppm), and elevated K_2O/Na_2O ratios (> 0.9). These characteristics are inconsistent with a direct mantle origin but the remelting of mafic lower crust ($Mg^{\#}$ 52–60, Pan et al. 2014) may produce suitable crust-derived magma. The crustal nature of the granodiorites is further supported by

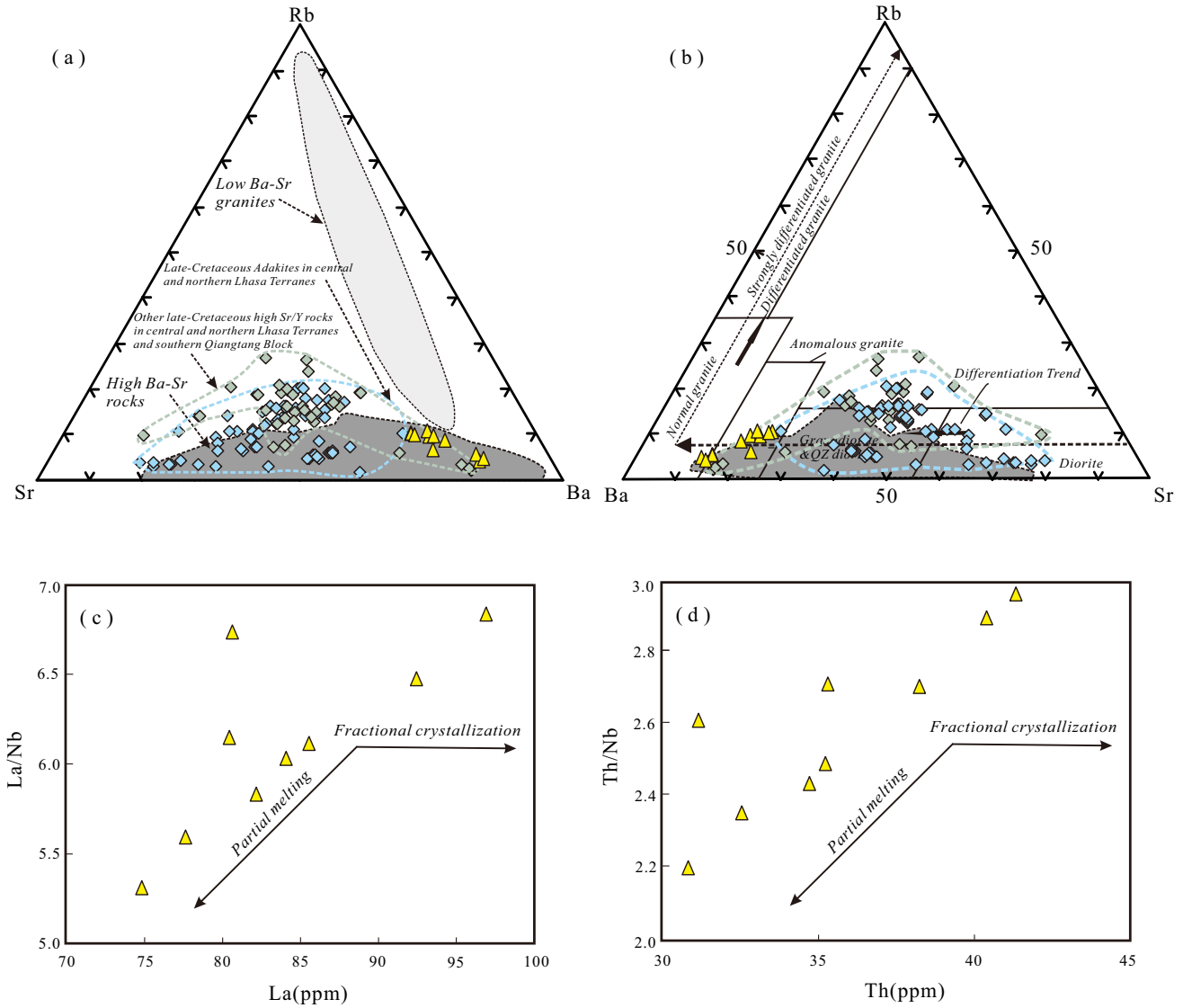

Fig. 6 **a** Sr–Rb–Ba (from Tarney and Jones 1994); **b** Rb–Ba–Sr; **c** La/Nb–La; and **d** Th/Nb–Th diagrams for the Late Cretaceous high Ba–Sr granodiorites in the SE Lhasa, China. Fields of low Ba–Sr granitoids are based on data data from Fowler and Henney (1996) and Fowler et al. (2001), other fields of high Ba–Sr, adakites and high Sr/Y rocks are based on data as same as in Fig. 4

the Fig. 5a, which exhibits depletion in P, Nb, and Ti, as well as enrichment in K and Sr, akin to those observed in average compositions of continental crust (Rudnick and Fountain 1995). Additionally, the Ce/Pb (7.3–8.7), Th/U (5.4–6.8), and Nb/U (2.2–2.7) ratios exhibit similarities to those observed in the lower continental crust (Foley et al. 2002). Experimental findings have indicated that partial melting mafic lower crust could generate magmas with elevated $(La/Yb)_N$ and Sr/Y ratios and weakly Eu anomalies at the condition of depth ≥ 40 km and pressure ≥ 1.2 GPa (Fig. 5 and 9) (Petford et al. 1996; Rapp and Watson 1995), with garnet in the residual assemblage (Petford and Gallagher 2001; Rapp et al. 1999, 2002). In summary, the petrogenesis of Yonglaga high Ba–Sr rocks can be attributed to partial melting of the mafic lower crust.

5.1.2 The magma source and decoupling of Hf and Nd isotope systems

Previous work demonstrated that the Nd–Hf isotope decoupling is common in the magmatic rocks of the SQT region during both the Early and Late Cretaceous periods (Sun et al. 2021; Wang et al. 2021). Our Sr–Nd–Hf isotopic signature is consistent with the range of granites

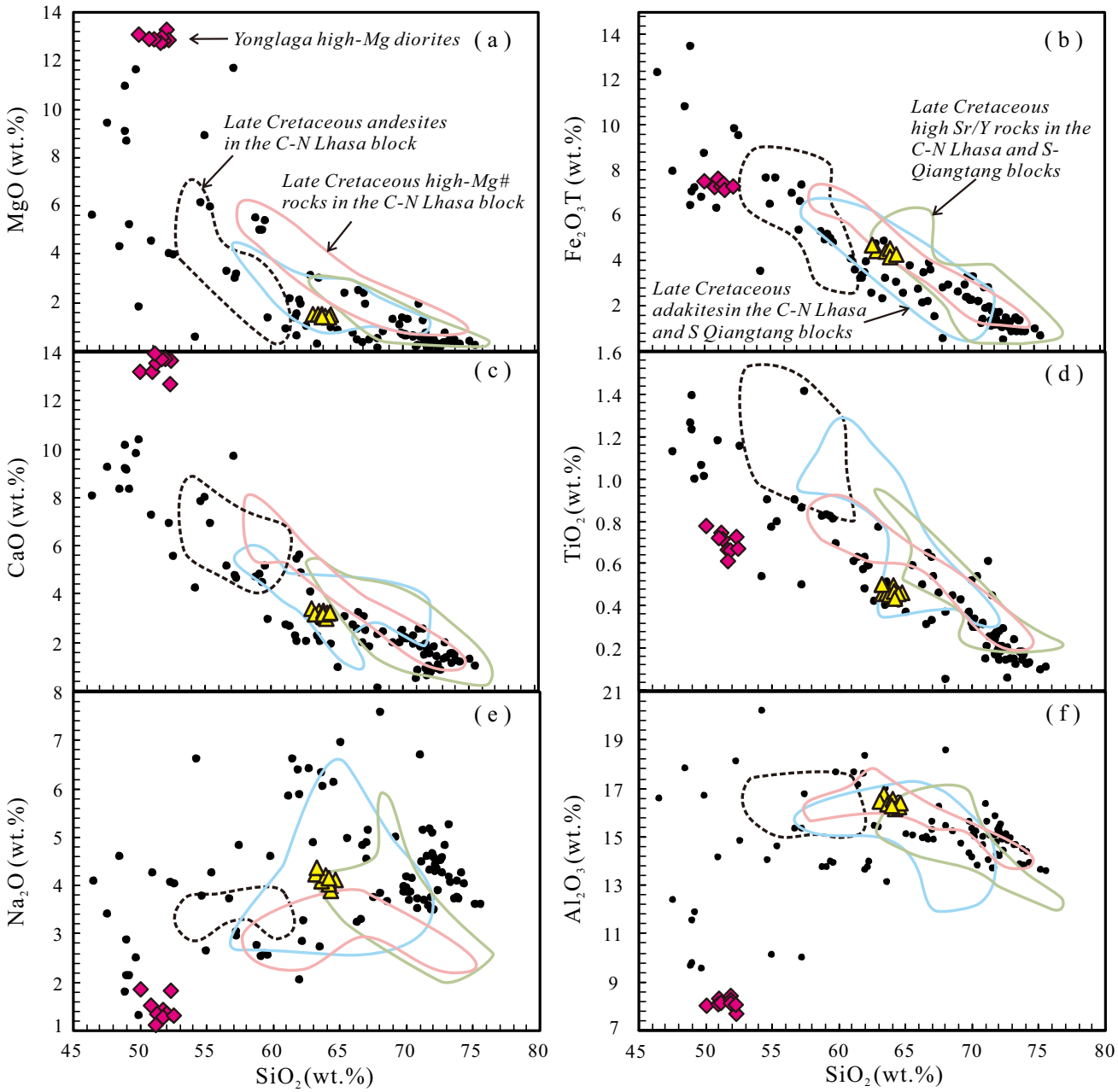

Fig. 7 The Harker diagram. The data of Late Cretaceous Yonglaga high-Mg basaltic rocks from Zhu et al. (2024). Symbols as in Fig. 4

and adakites in the SQT, CLT, and NLT during the Late Cretaceous, and also exhibits vital Nd–Hf isotope decoupling (Fig. 8). Magma resulting from partial melting of the ancient lower crust exhibits more depleted Sr–Nd isotopes and demonstrates limited decoupling between Nd and Hf isotopes [$\Delta\varepsilon$Hf(t) = 0.7–2.4; Sun et al. 2021]. In contrast, our granodiorites exhibit enriched initial $^{87}Sr/^{86}Sr$ (I_{Sr}) ranging from 0.707254 to 0.707322, negative εNd(t) values ranging from − 2.8 to − 3.6, and a range of εHf(t) values spanning from − 4.55 to + 13.01, indicating partial melting of the juvenile lower crust ($\Delta\varepsilon$Hf(t) = 3.0–10.3; Sun et al. 2021).

The negative bulk-rock εNd(t) values associated with positive εHf(t) values, together with the very different model ages derived from each isotopic system, signal unusual decoupling characteristics of Nd–Hf isotopic system (Chauvel et al. 2008, 2009). Disequilibrium melting processes and mantle source inheritance are both possible causes (Tang et al. 2014; Sun et al. 2020). Because our zircons are euhedral, prismatic and mostly have clear oscillatory zoning (Fig. 3a), the disequilibrium melting process is unlikely (Tang et al. 2014; Sun et al. 2021; Wang et al. 2021). However, Nd–Hf isotope decoupling can also indicate

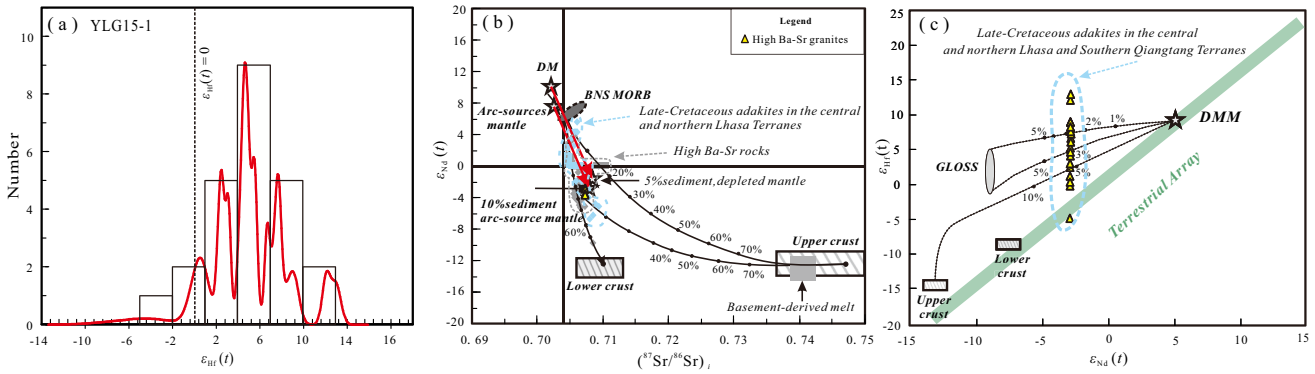

Fig. 8 **a** Histograms of initial Hf isotope ratios; **b** The εNd(t) values versus initial $^{87}Sr/^{86}Sr$ diagram for the high Ba–Sr Yonglaga granitoids in the SE Lhasa. The data of Depleted Mantle and Arc-sources mantle from Fowler et al. (2008). And BNS MORB data from Chen et al. (2014). Basement-derived melts (Zhu et al. 2011), lower continental crust (Miller et al. 1998), and upper continental crust (Harris et al. 1988). **c** The εNd(t) values versus εHf(t) values diagram. The terrestrial array is after Vervoort et al. (2011) [$\varepsilon Hf(t)=1.55\times\varepsilon Nd(t)+1.21$]. The Nd and Hf contents of depleted MORB mantle (DMM) (Workman and Hart 2005), global subducting sediment (GLOSS) (Plank 2014), lower crust (Rudnick and Gao 2014) and upper crust (Vervoort et al. 2011). The Nd/Hf isotopic compositions of DMM (Li et al. 2016), GLOSS [$\varepsilon Nd(t)=-8.9$, $\varepsilon Hf(t)=+2\pm3$] (Chauvel et al. 2008), lower crust (Hao et al. 2016) and upper crust (Vervoort et al. 2011)

a source involving subducted sediment. This model may be consistent with the genesis of the granodiorites which have noticeable Zr and Hf depletion plus variable zircon Hf isotopic compositions but consistent bulk Sr–Nd isotopes (Figs. 5a and 8c) (Tang et al. 2014). The "zircon effect" has also been used to interpret other igneous rocks during the Cretaceous. For example, the Namuqie granite [$I_{Sr}=0.7058$ to 0.7067, $\varepsilon Nd(t)=-1.1$ to -0.8, $\varepsilon Hf(t)=+2.7$ to $+9.5$] in the SQT, which is derived by partial melting of pre-existing juvenile arc crust involving a higher proportion of mature crust (20%–40%) (Wang et al. 2021). Another is the Duolong andesite in the SQT [$I_{Sr}=0.7045$–0.7071, $\varepsilon Nd(t)=-1.8$ to $+3.6$, $\varepsilon Hf(t)=+1.3$ to $+12.9$], which is derived from partial melting of the juvenile crust involving altered oceanic basaltic crust, mantle wedge peridotite, and subducted sediments (Sun et al. 2021). Thus, the spatial and temporal distributions of Yonglaga high Ba–Sr granodiorites are consistent with derivation by partial melting juvenile arc crust, indicating the similarity of the juvenile arc crust in the SE Lhasa and the SQT.

5.1.3 The reworking of metasomatized juvenile crust

The granodiorites have notably high K_2O contents (4.10wt%–4.82wt%), K_2O/Na_2O ratios (1.00–1.24), P_2O_5 contents (0.34wt%–0.41wt%), total REE (297–362 ppm) and LREE/HREE ratios (Fig. 4 and 5), indicating a shoshonitic affinity. High Ba–Sr and shoshonitic granitoids can be generated through analogous geological processes (Bersan et al. 2020; Tarney and Jones 1994; Fowler et al. 2008). The high Ba–Sr granites spatially overlap and adakitic rocks in SE Lhasa (Fig. 4, 5, and 9c, d). The Yonglaga granodiorites have relatively high Sr/Y (30.92–38.18) and $(La/Yb)_N$ (27.7–34.7) ratios, but they are not plotted into the field of adakitic rocks. There has been considerably debated, whether the high Sr/Y and $(La/Yb)_N$ geochemical indicators can accurately indicate crustal thickening (Moyen 2009; Wang et al. 2022a, b). The lack of significant correlations between SiO_2 and Sr/Y, as well as SiO_2 and Dy/Yb in the Yonglaga granodiorites suggests that the high Sr/Y (30.9–38.2) characteristic observed in the Yonglaga granodiorites cannot be solely explained by dominant processes like fractional crystallization involving garnet/amphibole, or by magma mixing. The derived melts from thickened crust will exhibit elevated Sr/Y and $(La/Yb)_N$ values with a positive correlation between La/Sm and Dy/Yb ratios (Wang et al. 2023). The lack of such a positive correlation in our samples suggests that the garnet-bearing thickened crust cannot be considered as the source of high Sr/Y characteristic. Therefore, the Yonglaga granodiorites have high Sr/Y and $(La/Yb)_N$ values, which can be attributed to inheritance from a magma source rather than crustal thickening (Moyen 2009). Further, for melting taking place within the rutile stability range, the resultant melts would display Nb/Ta ratios (> 16) that are higher than those of the source (Wang et al. 2023). Low Nb/Ta ratios (< 14) in Yonglaga samples suggest that the depletion of Nb, Ta, and Ti in Yonglaga granodiorites relates to derivation mafic arc lower crustal sources lacking residual rutile. On the other hand, the Yonglaga granodiorites exhibit fractionated LREE/HREE signature and discernable flat HREE-depleted patterns that supports the presence of residual garnet ± amphibole in the source (Patino-Douce 1999) (Figs. 5b and 10a, b).

The geochemical characteristics of the Yonglaga granodiorites are similar to post-collisional suites that have been affected by prior subduction events with subsequent

Table 4 Summary of some typical high Ba–Sr rocks in the world

Tectonic location	Pluton	Age (Ma)	Methods	Petrology	Geochemical characters	Isotopic ratios	References
North Atlantic/Scotland		425		Granite	High Ba, Sr, K/Rb, low Y and HREE, positive Sr and P, garnet residual		Tarney and Jones (1994)
Sutherland/Scotland		425		Appinites	High Ba, Sr, LREE, lack of Eu anomalies,	Lower initial $^{87}Sr/^{86}Sr$ and εNd(t), various and high $\delta^{18}O$	Fowler and Henney (1996)
Sutherland	Rogart pluton	425		Granite	Various MgO and SiO_2, high Na_2O+K_2O (up to 8.4wt%) and $K_2O/Na_2O\approx1.5$, similar trace element abundances with other typical high Ba–Sr pluton	Lower initial $^{87}Sr/^{86}Sr$ and relative high and positve εNd(t), and high $\delta^{18}O$	Fowler et al. 2001)
Scotland	Northern Highland	425		Granite-syenite			Fowler et al. (2008)
Eastern Tibet	Yulong	38.9	Zircon SHRIMP U–Pb	Monzogranite-porphyry	Shoshonitic affinity, alkalis-rich, rich in LREE and LILE, high Sr/Y and La/Yb, no Eu anomalies	Low initial $^{87}Sr/^{86}Sr$ and slightly negative εNd(t), posoitve $\varepsilon Hf(t)\approx+4$–5	Jiang et al., (2006)
Western Kunlunorogenic belt	Buya	430	Zircon SHRIMP U–Pb	Appinite-granite	High SiO_2 and Na_2O+K_2O, high Ba. Sr, LREE, Sr/Y and La/Yb, low HREE and HFSE, insignificant Eu anomalies	Negative $\varepsilon Nd(t)=-8.4$ to -10.4	Ye et al. (2008)
Western Tibet	Karibasheng and Kuzigan	12–10	Zircon SHRIMP U–Pb	Granite	Shoshonitic with high K_2O and Na_2O (alkaline), rich in LILE and LREE, low in HFSE and HREE	Lower initial $^{87}Sr/^{86}Sr$ and negative $\varepsilon Nd(t)=-7.1$ to -9.5 and $\varepsilon Hf(t)\approx-7.2$ to -9.7	Jiang et al. (2012)
Eastern China	Taishan	~2500	Zircon LA-ICP-MS U–Pb	Granite	Alkaline-rich, rich in LILE and LREE, negative in HFSE(Nb, Ta, Ti), insignificant Eu anomalies, fractionated REE and high Sr/Y	Elevated εNd(t) and zircon Hf(t) compositions	Peng et al. (2013)

Table 4 (continued)

Tectonic location	Pluton	Age (Ma)	Methods	Petrology	Geochemical characters	Isotopic ratios	References
Northern China Craton	Badaling	Mesozoic	Zircon LA-ICP-MS U–Pb	Gabbroic to granitic rocks	Various MgO and SiO_2, high $Na_2O + K_2O$, similar trace element abundances with other typical high Ba–Sr pluton	EMI type Sr–Nd isotopes (intial Sr = 0.7051–0.7068 and εNd(t) = − 8.2 to − 20.2)	Qian et al. (2002)
South Korea	Hongseong belt	233	Zircon SHRIMP U–Pb	Granites	High-K, calc-alkaline, high LREE/HREE, absence of a negative Eu	High $\delta^{18}O$	Choi et al. (2009)
SE Lhasablock	Yonglaga Pluton	87.3 ± 0.4	Zircon LA-ICP-MS U–Pb	Granodiorites	Shoshonitic affinity, alkaline-rich, similar Trace element characters with other high Ba–Sr rocks	Zircon εHf(t) = − 4.5 to + 13.0	This study

metasomatism of the lithospheric mantle. The granodiorites have high Ba/Y (60.2–74.8) and low Nb/Y ratios (0.60–0.70), suggesting the influence of fluid-related metasomatism (Fig. 10c). Similarly, the $(Hf/Sm)_N$ versus $(Ta/La)_N$ diagram also shows that the source has undergone fluid-related metasomatism (Fig. 10d). Therefore, the high-K calc-alkaline to shoshonitic affinity and high Ba–Sr signature of our samples can be explained by fluid-related metasomatism in the mantle source of the parent mafic magmas.

The contribution of mature crustal material in the mantle source is further evidenced by the uniformly enriched Sr–Nd isotopes [$I_{Sr} = 0.707254–0.707322$, $\varepsilon Nd(t) = -2.8$ to -3.6], similar to high Ba–Sr rocks from the Caledonian in British which have been explained by mixing between depleted-enriched mantle and 5%–10% sediment (Fowler et al. 2008, noted on Fig. 8b). The high Th/Yb (15.2–20.7) and La/Sm (10.3–12.9) ratios in Yonglaga granodiorites also indicate a significant contribution from subducted sediments in their metasomatized source (Bersan et al. 2020). The presence of low Lu/Hf (0.05–0.06) ratios combined with elevated Th/La (0.38–0.49) and Th/Yb (15.3–20.8) implies the dominance of terrigenous contributions rather than pelagic inputs (Fig. 9a and b). The reaction between terrigenous sediment and dunite leads to the formation of phlogopite pyroxenites, which could produce high-K melts with enriched LILEs (Förster et al. 2019). In addition, the carbonate or carbonatite involvement to explain the significant increase in Sr (~ 1000 ppm) and LREE (La/Yb approximately 10) has been proposed (Fowler et al. 2008; Tarney and Jones 1994). The relatively high P_2O_5 values (0.34wt%–0.41wt%) in our samples well support the possibility of carbonatite metasomatism (Rudnick et al. 1993).

In summary, the reworking of the juvenile mafic arc lower crust (amphibolite source) constitutes a plausible mechanism for generating the potassic high Ba–Sr Yonglaga granodiorites. The juvenile mafic crust itself was formed through the melting of subduction-related metasomatized mantle, including a contribution of terrigenous sediments.

5.2 Geodynamic implications

An increasing amount of post-collision silicic magmatism has been discovered to be associated with continental growth, particularly the high Ba–Sr granitoids derived from the mantle (Gómez-Frutos et al. 2023; Fowler et al. 2008). However, the significance of the relationship between crust-derived high Ba–Sr granitoid and continental growth is often overlooked due to its indirect association. Numerous Late Cretaceous granitoids (ca. 120–100 Ma), derived from the melting of juvenile crust, have been documented in the SQT (Li et al. 2013; Liu et al. 2014, 2017; Sun et al. 2021). The Yonglaga granodiorites show similar zircon Hf isotopic signature ($\varepsilon Hf(t)$ values = − 4.55 to + 13.01) with these ($\varepsilon Hf(t)$

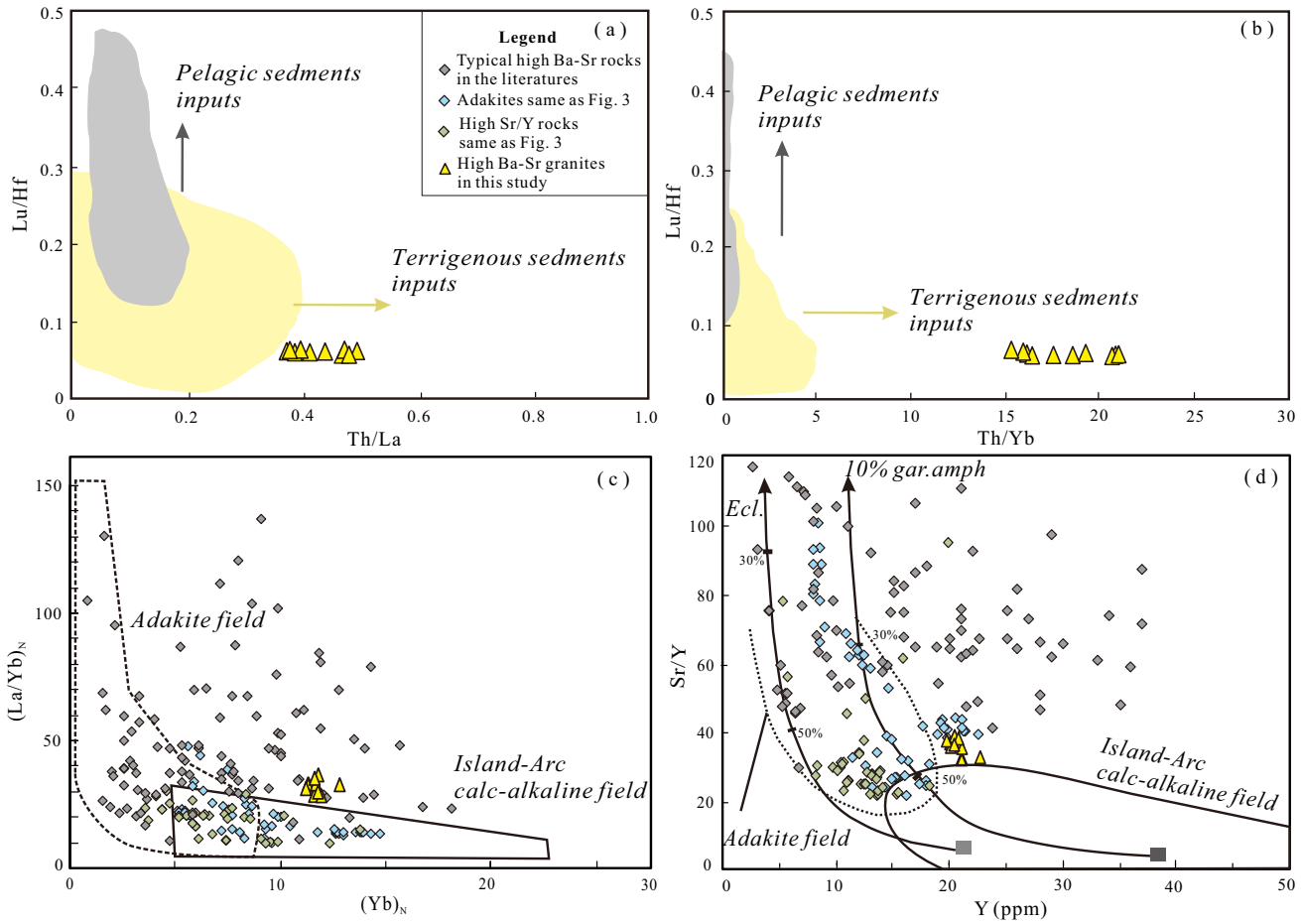

Fig. 9 Lu/Hf versus Th/La and Lu/Hf versus Th/Yb diagram (**a**, **b**) (from Zhu et al. 2023). Light grey represents oceanic arc magmas with pelagic sediment input and light yellow represents continental arc magmas with terrigenous sediment input. Associated data from GEOROC (http://georoc.mpch-mainz.gwdg.de/georoc). The $(La/Yb)_N$ versus $(Yb)_N$ and Sr/Y versus Y diagram (**c**, **d**). The yellow rectangular symbols represent the high Ba–Sr granites in this study. The light grey rectangular symbols are for high Ba–Sr rocks in different terranes of the world. The light blue symbols are Late Cretaceous adakites in the central and northern Lhasa terranes and the lightly green are other Late Cretaceous high Sr/Y rocks in the central and northern Lhasa and southern Qiangtang terranes

values = − 1.3 to + 13.6), suggesting the presence of similar juvenile crust in SE Lhasa (Liu et al. 2014, 2017). Sun et al. (2021) have argued that the juvenile lower crust in the SQT is a mélange of MORB, mantle wedge peridotites, and subducted sediments. The melting of such mélange protoliths plays an important role in Nd–Hf isotopic decoupling and adakitic characteristics observed in the Late Cretaceous SQT rocks. Although there are recycled sediments at the source, the dominant depleted zircon Hf isotopic composition still implies significant crustal growth.

The petrogenesis of Yonglaga high Ba–Sr granodiorites and the closure of BNTO studies indicate the occurrence of post-collision extension during the Late Cretaceous in SE Lhasa (Hu et al. 2022; Kapp et al. 2005, 2007). According to the extensional setting, upwelling of asthenosphere mantle material could cause partial melting of the lithospheric mantle and result in the formation of mafic magma. The Late Cretaceous Yonglaga basaltic rocks represent underplated mafic magma in the lower crust, which could provide a significant amount of heat that leads to partial melting of the juvenile crust and subsequently resulting in the formation of granodiorite (Zhu et al. 2024). The whole-rock Zr saturation temperature (794–805 ℃) of the Yonglaga granodiorites further indicates the contribution of underplated mafic magma.

A model involving lithospheric delamination has been widely proposed to explain the post-collisional magmatic activity, in accordance with the inferred crustal thickening during the Late Cretaceous (He et al. 2019; Li et al. 2013; Lu et al. 2019). Abundant adakitic rocks with high Mg and/or $Mg^{\#}$ have been found in central Xizang (Table 5, Fig. 1a), including the NLT and CLT (Cao et al. 2022; Chen et al. 2015; Li et al. 2013; Ma and Yue 2010; Meng et al. 2014; Qu et al. 2006; Sun et al. 2015a, 2020; Wang et al. 2014; Yu et al. 2011; Yi et al. 2018; Zhao et al.

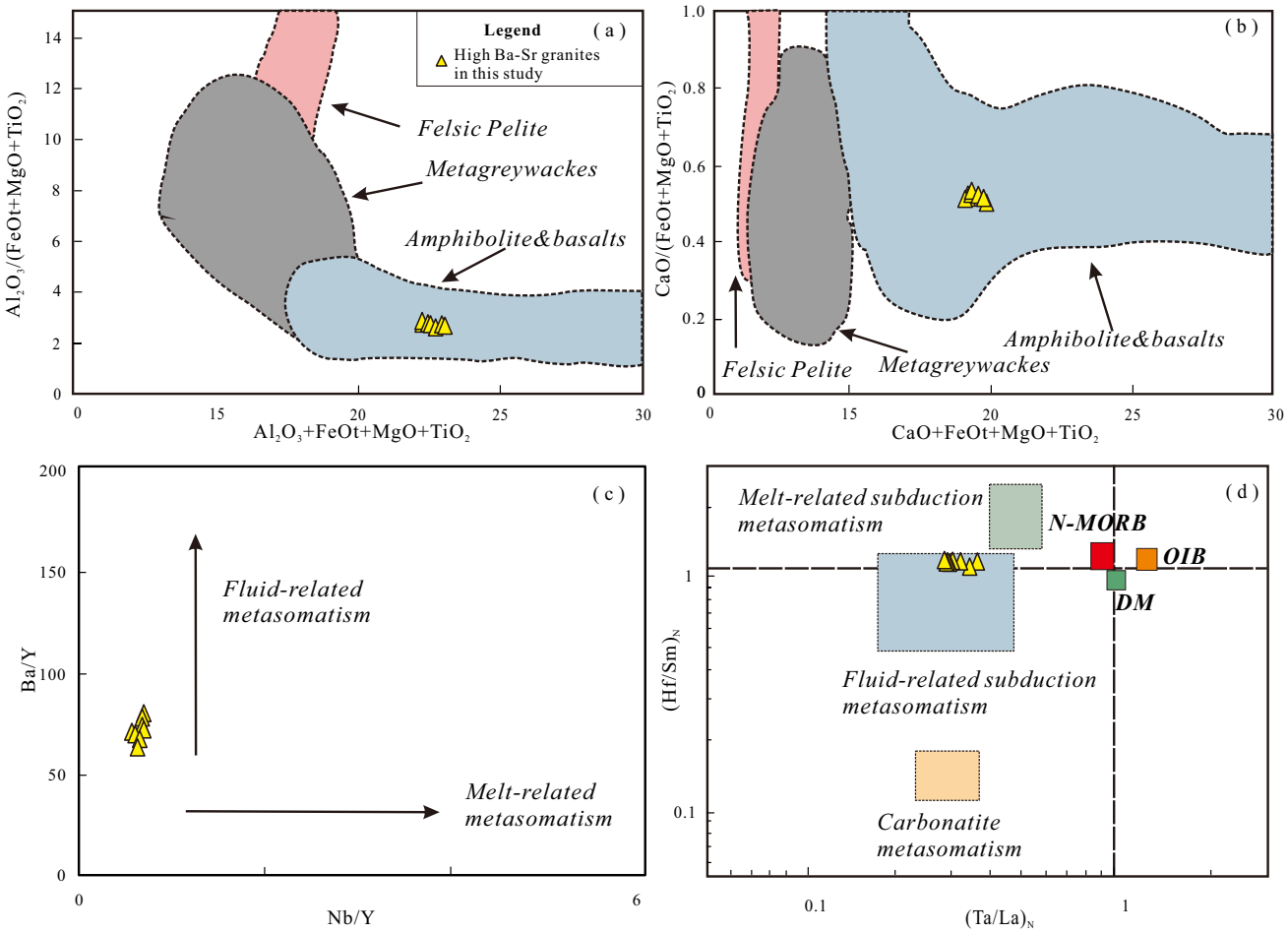

Fig. 10 Major element compositions (wt%) of the Yonglaga high Ba–Sr granodiorites plotted as a ratio between two variables vs. the sum of the same variables (**a**, **b**). Compositions of melts generated experimentally by dehydration melting of a wide range of bulk compositions (Patiño Douce 1999). The Ba/Y versus Nb/Y and $(Hf/Sm)_N$ versus $(Ta/La)_N$ diagram (**c**, **d**) (La Flèche et al. 1998)

2008), and SQT (Li et al. 2013, 2016; Liu et al. 2014, 2017). These have significantly positive zircon Hf isotope signatures, suggesting a depleted mantle source. Recent studies have provided evidence for a westward migration of small-scale lithospheric delamination from the CLT and NLT and the SQT during this period (Li et al. 2016; Wang et al. 2023; Yi et al. 2018). A plausible geodynamic mechanism is lithospheric foundering by Rayleigh–Taylor instability (Houseman and Molnar 1997; Li et al. 2016; Yi et al. 2018). Sun et al. (2020) have demonstrated that localized mantle convection has partially eradicated the lithospheric mantle keel, leading to crustal and lithospheric mantle thinning during the LT and SQT collision. Such partial lithospheric delamination would have resulted in an increased geothermal gradient within the lithospheric mantle, thereby inducing the melting of the thinned crust. However, the Yonglaga granodiorites and coeval mafic rocks do not show adakitic signature (Polat and Kerrich 2001; Zhu et al. 2024). As above mentioned, the petrogenesis of the Yonglaga granodiorites shows that the crust thickness was normal in SE Lhasa during the Late Cretaceous. In addition, few reports of adakites in the SE Lhasa regionally. When the lithosphere undergoes delamination, the thinned crust becomes more susceptible to partial melting and results in the formation of large areas of magmatic rocks, but the scattered and small-volume igneous rocks are distributed in the SE Lhasa. Therefore, our study did not uncover any evidence to support the mechanism of both crust thickening and delamination in the SE margin of Lhasa. It is worth noting that our samples exhibit similar Hf isotopic characteristics to coeval adakites in the CLT and NLT (Fig. 11a), indicating that the similar source from the juvenile crust. But the relative lower $(La/Yb)_N$ (27.7–34.7) and Sr/Y (30.9–38.2) ratios than coeval adakites derived from partial melting thickened lower crust in CLT and NLT, our samples also are plotted out of the field of adakitic rocks (Figs. 9c, d and 11b). Thus, it could be not inferred the crust thickening

Table 5 Summary of Late Cretaceous magmatisms in the central and northern Lhasa Terranes and southern Qiangtang block

Location	Samples	Rock type	Dating method	Age (Ma)	Geochemical affinity	Zircon $\varepsilon_{Hf}(t)$	References
Central Lhasa Terrane	11BG01-1	Dacite	Zircon LA-ICP-MS U–Pb	93.8 ± 0.8	High Mg# and adakitic affinity	(+8.3 to 12.4)	Yi et al. (2018)
	ZC-18	Granitoids	Zircon LA-ICP-MS U–Pb	90.7 ± 1.3	High Mg# and adakitic affinity		Chen et al. (2015)
	LS-P	Rhyodacites/dacites	Zircon LA-ICP-MS U–Pb	89.8 ± 0.9	High Mg# and adakitic affinity	(+8.90 to + 15.98)	Sun et al. (2015a)
	LS-74	Rhyodacites/dacites	Zircon LA-ICP-MS U–Pb	86.8 ± 0.9			
	MB14-4	Granite	Zircon LA-ICP-MS U–Pb	83.7 ± 0.5	High Mg# and adakitic affinity	(−7.50 to −0.2)	Meng et al. (2014)
	MB14-2	Dioritic enclave	Zircon LA-ICP-MS U–Pb	85.2 ± 0.4			
	CQRA09-7	Granite	Zircon LA-ICP-MS U–Pb	89.9 ± 1.6	High Mg# and Sr/Y ratios		Yu et al. (2015)
	ZGP06-1	Dacite	Zircon SHRIMP U–Pb	91.0 ± 0.8	High Mg and adakitic affinity	(+5.6 to + 8.7)	Wang et al. (2014)
	RT1	Granite	Zircon LA-ICP-MS U–Pb	80.0 ± 1.2	High MgO and Mg#, high Sr/Y		Zhao et al. (2008)
	RT7	Granite	Zircon LA-ICP-MS U–Pb	79.4 ± 0.9			
	JB17-03	Andesite	Zircon LA-ICP-MS U–Pb	87.1 ± 1.1	High MgO and Mg#, high Sr/Y	(+2.7 to + 5.4)	Sun et al. (2020)
	JB16-04	Dacite	Zircon LA-ICP-MS U–Pb	85.1 ± 1.0	High MgO and Mg#, high Sr/Y	(+2.7 to + 7.1)	
	JB17-08	Rhyolite	Zircon LA-ICP-MS U–Pb	81.6 ± 0.5	non-adakitic signatures and low Mg#	(+1.0 to + 3.5)	
Northern Lhasa Terrane	NSB1	Quartz diorite	Zircon LA-ICP-MS U–Pb	87.1 ± 0.4	High Sr/Y and adakitic affinity		Yao et al. (2013)
	CR16	Monzonitic granite Porphyry	Zircon LA-ICP-MS U–Pb	90.1 ± 1.5	High Mg# and adakitic affinity		Qu et al. (2006)
	CR27	Diabase	Zircon LA-ICP-MS U–Pb	87.2 ± 1.6			
	PM95-15	Quartz monzonite	Zircon LA-ICP-MS U–Pb	85.60 ± 0.48	High Mg# and adakitic affinity		Li et al. (2013)
		Iron-deposition	Zircon LA-ICP-MS U–Pb	85.51 ± 0.77			
	09ZC-15	Granodiorite	Zircon LA-ICP-MS U–Pb	92.1 ± 1.2			Wang et al. (2013)
	09ZC-02	Granodiorite	Zircon LA-ICP-MS U–Pb	93.8 ± 1.2			
	ZC17	Porphyry granite	Zircon LA-ICP-MS U–Pb	88.0 ± 1.6	High Mg# and adakitic affinity		Yu et al. (2011)
	GJ-15	Granodiorite	Zircon LA-ICP-MS U–Pb	86.59 ± 0.49	S-type granites		Lu et al. (2011)
	GJ-37	Diorite	Zircon LA-ICP-MS U–Pb	88.99 ± 0.45			
	GJ-38	Diorite	Zircon LA-ICP-MS U–Pb	88.74 ± 0.74			
	2003T468	Volcanic rocks	Hornblende 40Ar/39Ar	91.2 ± 0.2	High Mg and Zr/Y, within-plate basalt affinity		Ma and Yue. (2010)
		Volcanic rocks	Rb–Sr	91.0 ± 0.6			
	DC-29	Andesites and rhyolite	Zircon LA-ICP-MS U–Pb	94 ± 1	High Sr/Y and adakitic affinity		Haider et al. (2013)

Table 5 (continued)

Location	Samples	Rock type	Dating method	Age (Ma)	Geochemical affinity	Zircon $\varepsilon_{Hf}(t)$	References
	YLG15-1	Granite	Zircon LA-ICP-MS U–Pb	87.3 ± 0.4	High Ba–Sr and Sr/Y ratios	(−4.5 to + 13.0)	This study
	L-6	Andesite	Zircon LA-ICP-MS U–Pb	79.9 ± 2.7	K-rich high Sr/Y	(−5.8 to + 0.9)	Li et al. (2013)
	L-6–01	Andesite	Zircon LA-ICP-MS U–Pb	75.9 ± 0.49			
	MDH-U40	Volcanic rocks	Zircon LA-ICP-MS U–Pb	100.8 ± 0.9	High Sr/Y		Li et al. (2016)
	MDH-U29	Volcanic rocks	Zircon LA-ICP-MS U–Pb	102.6 ± 1.6			
	EU-3	Volcanic rocks	Zircon LA-ICP-MS U–Pb	96.1 ± 2.4			
	EU-5	Volcanic rocks	Zircon LA-ICP-MS U–Pb	100.4 ± 1.1			
Southern Qiangtang block	08058B	Bt-Hbl monzogranite	Zircon LA-ICP-MS U–Pb	93.3	High Mg# and high Sr/Y	(+4.5 to + 9.5)	Liu et al. (2017)
	08059B	Bt-Hbl monzogranite	Zircon LA-ICP-MS U–Pb	83.7			
	8057	Bt-Hbl monzogranite	Zircon LA-ICP-MS U–Pb	101		(+4.5 to + 8.9)	
	08058A	Bt-Hbl monzogranite	Zircon LA-ICP-MS U–Pb	101		(+1.4 to + 13.6)	
	09019–1	Granite	Zircon LA-ICP-MS U–Pb	104		(−1.0 to + 5.7)	
	21-DM-02	Rhyolite	Zircon LA-ICP-MS U–Pb	98.3 ± 0.61	High-K calc-alkaline series	(−0.7 to + 2.7)	Wen et al. (2023)
	16DM17-1	Granite porphyries	Zircon SHRIMP U–Pb	76.00 ± 0.61	Calc-alkaline peraluminous	(+9.9 to + 12)	Wang et al. (2021)
	17NMQ01-5	Granite porphyries	Zircon SHRIMP U–Pb	78.85 ± 0.87	Calc-alkaline strongly peraluminous	(+5.3 to + 6.6)	
	17NMQ04-9	Granite porphyries	Zircon SHRIMP U–Pb	78.15 ± 0.61		(+7.0 to + 7.4)	
	AD-16–2	Volcanic rocks	Zircon LA-ICP-MS U–Pb	79.6 ± 0.8	High Mg# and adakitic affinity	(−1.3 to + 1.4)	Ji et al. (2021)

setting but implies the normal crustal setting in the SE Lhasa terrane. Considering that our samples were collected from the SE margin of the Lhasa terrane, a heterogeneous crustal thickness could have occurred during the Late Cretaceous. The central and northern parts of the Lhasa terrane are thickened but the SE margin could be normal (Fig. 12a).

Recently, the extension could have been driven by the far-field effects of subduction of the Neo-Tethys oceanic crust (Wang et al. 2019, 2021). The BN slab break-off during the Late Cretaceous (~ 110 Ma) and driven by the far-field subduction of the Neo-Tethys oceanic crust (Chapman et al. 2018). The roll-back of the Neo-Tethyan oceanic slab during the Late Cretaceous (~ 85 Ma) could result in scattered and small-volume igneous rocks in the LT and SQT (Wang et al. 2021). In addition, most of the Late Cretaceous felsic igneous rocks are found from the SQT to the Gangdese zone. They were formed at various magmatic temperatures (600–900 °C), indicating that their formation could have been controlled by the mechanism of the Neo-Tethyan oceanic slab (Wang et al. 2021). This mechanism has caused the reworking of juvenile crust and triggered shoshonitic magmatism in central and eastern Lhasa during the Late Cretaceous, which is consistent with the sporadic occurrence and limited volume of Late Cretaceous (ca. 100–80 Ma) magmatic rocks in the SE Lhasa (Wang et al. 2019, 2021).

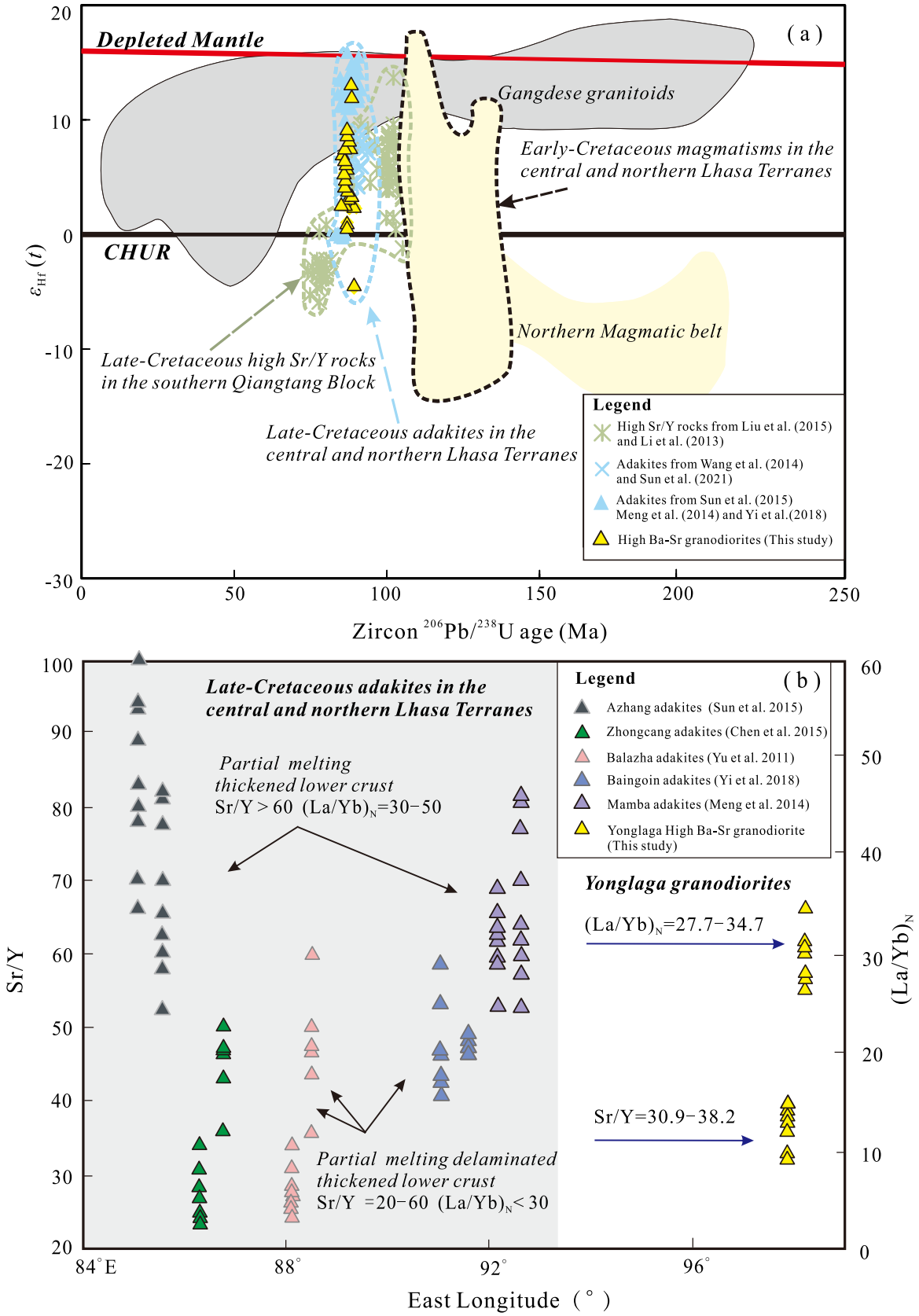

Fig. 11 **a** The Zircon Hf components vs. zircon U–Pb data of in the central and northern Lhasa and southern Qiangtang terranes; **b** the Sr/Y and $(La/Yb)_N$ ratios versus longitude data of Late Cretaceous adakites and high Ba–Sr granodiorites in Lhasa terrane

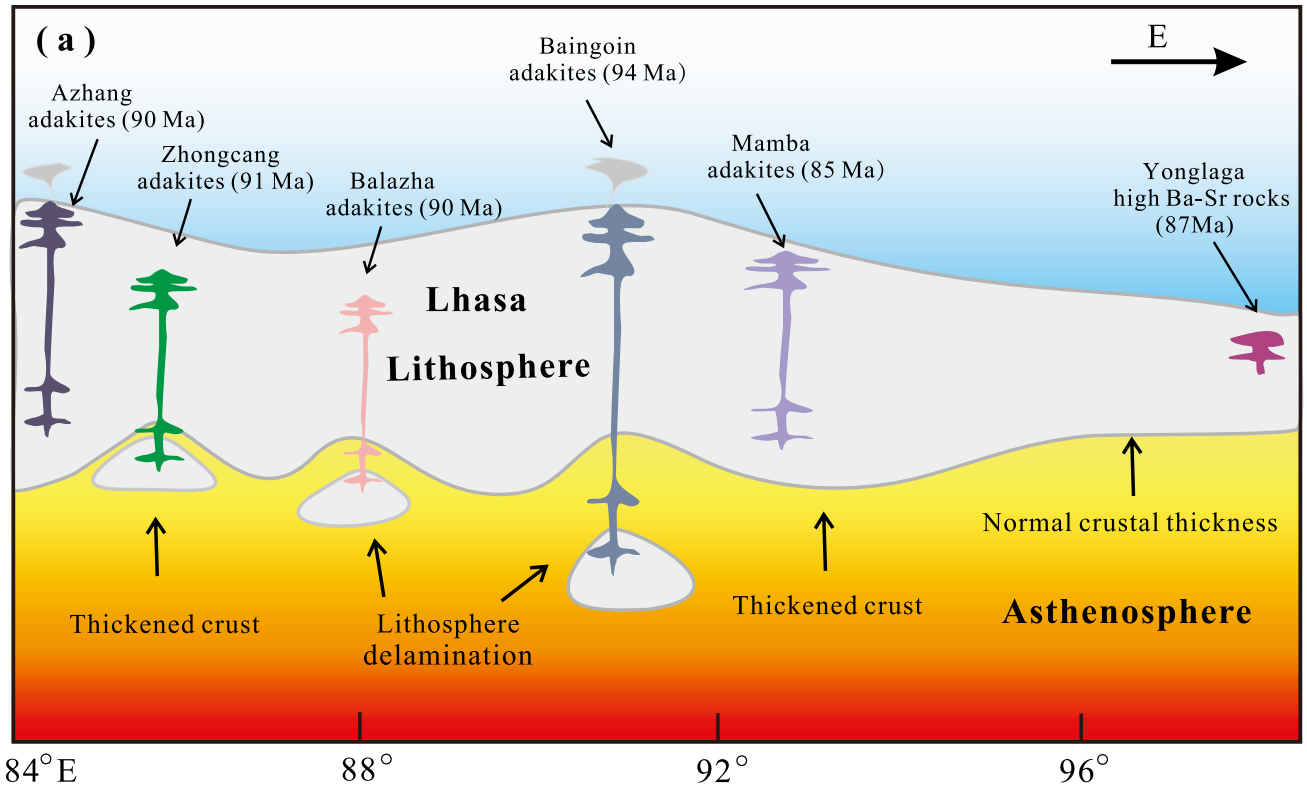

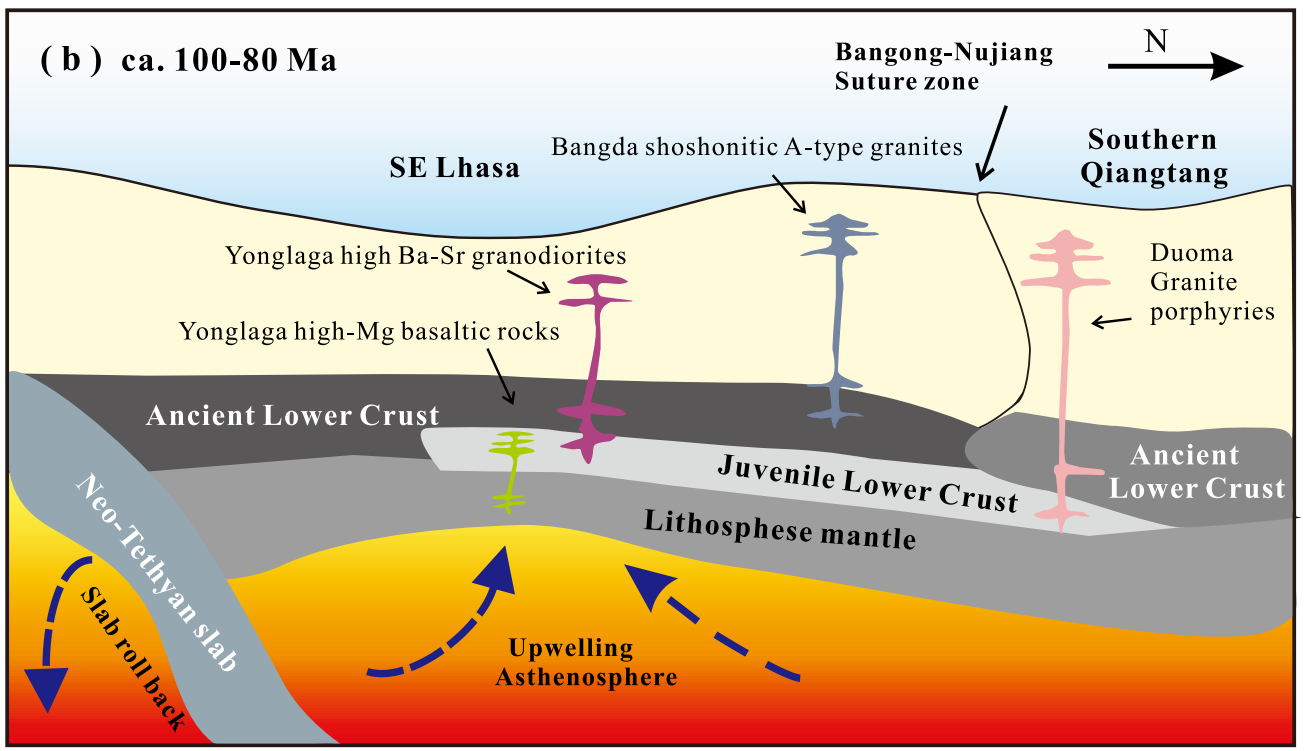

Fig. 12 **a** The model of the Late Cretaceous magmatism in the Lhasa terrane; **b** the model of the Late Cretaceous magmatism in the Lhasa and southern Qiangtang terranes following final Lhasa-Qiangtang amalgamation

Therefore, the far-field effect of Neo-Tethyan oceanic slab roll-back during the Late Cretaceous period could lead to crustal melting and thus result in the formation of the Yonglaga high Ba–Sr granodiorites (Fig. 12b).

6 Conclusions

(1) The high Ba–Sr granodiorites were emplaced at 87 Ma, derived from the reworking of the juvenile mafic arc lower crust that itself formed by melting of metasomatized mantle.
(2) Their isotopic characteristics are similar to the coeval juvenile crust-derived magmatic rocks in the southern Qiangtang terrane, suggesting that the decoupled Nd–Hf isotopic system has been inherited from a complexly metasomatized mantle source, which implies the growth of continental crust.
(3) The underplated mafic magma provides a significant amount of heat, leading to partial melting of the juvenile crust and subsequently formation of the high Ba–Sr granodiorite.
(4) Both the Late Cretaceous adakitic rocks and high Ba–Sr granodiorites have similar juvenile crustal sources, but they could be derived from heterogeneous thickness. There is crustal thickening and delamination in the center of the Lhasa terrane, and the crust thickness remains normal at the SE margin.
(5) The Late Cretaceous igneous rocks in Yonglaga were formed in a post-collisional extensional setting, which was possibly triggered by the far-field effects of the subduction of the Neo-Tethyan oceanic crust.

Acknowledgements We wish to thank the editor Dr. Binbin Wang for handling the manuscript and Hamed Gamaleldien and other anonymous reviewers' constructive comments. This study was jointly supported by the National Natural Science Foundation of China (Grants No. 41802054) and supported by a Royal Society Sino-British Fellowship Trust International Exchanges Award (Grant No. IES\R3\213093).

Author contributions R.Z.Z. and L.H.L. designed the projects. L.H.L. M.L. S.W.Z. and R.Z.Z. conducted fieldwork and performed the whole geochemical and isotopic analysis. R.Z.Z. and L.H.L. wrote the initial manuscript. Y.Z., S.C.L., M.L. and J.F.Q. contributed to the data interpretation and final version of manuscript.

Funding This study was jointly supported by the National Natural Science Foundation of China [Grants. 41802054] and also supported by a Royal Society SinoBritish Fellowship Trust International Exchanges Award [Grant No. IES\R3\213093].

Data availability The authors confirm that the data supporting the findings of this study are available within the article [and/or its supplementary materials].

Declarations

Conflict of interest We declare that we do not have any commercial or associative interest that represents a conflict of interest in connection with the work submitted.

References

Andersen T (2002) Correction of common lead in U-Pb analyses that do not report ^{204}Pb. Chem Geol. 192(1–2):59–79. https://doi.org/10.1016/s0009-2541(02)00195-x

Bersan SM, de Oliveira Costa AF, Danderfer A, de Abreu FR, Lana C, Queiroga G, Storey C, Moreira H (2020) Paleoproterozoic juvenile magmatism within the northeastern sector of the São Francisco paleocontinent: Insights from the shoshonitic high Ba–Sr Montezuma granitoids. Geosci Front. 11(5):1821–1840. https://doi.org/10.1016/j.gsf.2020.01.017

Cao Y, Kang Z, Yang F, Zhou T, Liu D, Wang R (2022) Geochronology, geochemistry and geological significance of volcanic rocks of the Bangba district, western segment of the central Lhasa Subterrane. Journal of Earth Science. 33(3):681–695. https://doi.org/10.1007/s12583-022-1634-0

Chapman JB, Scoggin SH, Kapp P, Carrapa B, Ducea MN, Worthington J, Oimahmadov I, Gadoev M (2018) Mesozoic to Cenozoic magmatic history of the Pamir. Earth Planet Sci Lett. 482:181–192. https://doi.org/10.1016/j.epsl.2017.10.041

Chauvel C, Lewin E, Carpentier M, Arndt NT, Marini JC (2008) Role of recycled oceanic basalt and sediment in generating the Hf–Nd mantle array. Nat Geosci. 1(1):64–67. https://doi.org/10.1038/ngeo.2007.51

Chauvel C, Jean-Christophe M, Terry P, Ludden JN (2009) Hf-Nd input flux in the Izu-Mariana subduction zone and recycling of subducted material in the mantle. Geochem Geophys Geosyst. 10(1):514–527. https://doi.org/10.1029/2008gc002101

Chen Y, Zhu DC, Zhao ZD, Meng FY, Wang Q, Santosh M, Wang LQ, Dong GC, Mo XX (2014) Slab breakoff triggered ca. 113Ma magmatism around Xainza area of the Lhasa Terrane, Tibet. Gondwana Res. 26(2):449–463. https://doi.org/10.1016/j.gr.2013.06.005

Chen J, Xu J, Yu H, Wang B, Wu J, Feng Y (2015) Late Cretaceous high-Mg# granitoids in southern Tibet: Implications for the early crustal thickening and tectonic evolution of the Tibetan Plateau? Lithos. 232:12–22. https://doi.org/10.1016/j.lithos.2015.06.020

Chiu HY, Chung SL, Wu FY, Liu D, Liang YH, Lin IJ, Iizuka Y, Xie LW, Wang Y, Chu MF (2009) Zircon U-Pb and Hf isotopic constraints from eastern Transhimalayan batholiths on the precollisional magmatic and tectonic evolution in southern Tibet. Tectonophysics. 477(1–2):3–19. https://doi.org/10.1016/j.tecto.2009.02.034

Choi S, Rajesh VJ, Seo J, Park J, Oh C, Pak S, Kim S (2009) Petrology, geochronology and tectonic implications of Mesozoic high Ba–Sr granites in the Haemi area, Hongseong Belt. South Korea Island Arc. 18(2):266–281. https://doi.org/10.1111/j.1440-1738.2008.00622.x

Chu MF, Chung SL, Song B, Liu D, O'Reilly SY, Pearson NJ, Ji J, Wen DJ (2006) Zircon U-Pb and Hf isotope constraints on the Mesozoic tectonics and crustal evolution of southern Tibet. Geology. 34(9):745–748. https://doi.org/10.1130/g22725.1

Chu ZY, Chen FK, Yang YH, Guo JH (2009) Precise determination of Sm, Nd concentrations and Nd isotopic compositions at the nanogram level in geological samples by thermal ionization mass

spectrometry. J Anal at Spectrom. 24(11):1534–1544. https://doi.org/10.1039/b904047a

DeCelles PG, Kapp P, Ding L, Gehrels GE (2007) Late Cretaceous to middle tertiary basin evolution in the central Tibetan Plateau: Changing environments in response to tectonic partitioning, aridification, and regional elevation gain. Geol Soc Am Bull. 119(5–6):654–680. https://doi.org/10.1130/b26074.1

Foley S, Tiepolo M, Vannucci R (2002) Growth of early continental crust controlled by melting of amphibolite in subduction zones. Nature. 417(6891):837–840. https://doi.org/10.1038/nature00799

Förster MW, Prelević D, Buhre S, Mertz-Kraus R, Foley SF (2019) An experimental study of the role of partial melts of sediments versus mantle melts in the sources of potassic magmatism. J Asian Earth Sci. 177:76–88. https://doi.org/10.1016/j.jseaes.2019.03.014

Fowler MB, Henney PJ (1996) Mixed Caledonian appinite magmas: Implications for lamprophyre fractionation and high Ba–Sr granite genesis. Contrib Miner Petrol. 126(1–2):199–215. https://doi.org/10.1007/s004100050244

Fowler MB, Henney PJ, Darbyshire DF, Greenwood PB (2001) Petrogenesis of high Ba–Sr granites: The Rogart pluton, Sutherland. J Geol Soc. 158(3):521–534. https://doi.org/10.1144/jgs.158.3.521

Fowler MB, Henney PJ, Darbyshire DPF, Greenwood PB (2008) Petrogenesis of high Ba–Sr plutons from the northern highlands terrane of the British Caledonian province. Lithos. 105(1–2):129–148. https://doi.org/10.1016/j.lithos.2008.03.003

Gómez-Frutos D, Castro A, Gutiérrez-Alonso G (2023) Post-collisional batholiths do contribute to continental growth. Earth Planet Sci Lett. 603:117978. https://doi.org/10.1016/j.epsl.2022.117978

Goolaerts A, Mattielli N, de Jong J, Weis D, Scoates JS (2004) Hf and Lu isotopic reference values for the zircon standard 91500 by MC-ICP-MS. Chem Geol. 206(1–2):1–9. https://doi.org/10.1016/j.chemgeo.2004.01.008

Guynn JH, Kapp P, Pullen A, Heizler M, Gehrels G, Ding L (2006) Tibetan basement rocks near Amdo reveal "missing" Mesozoic tectonism along the Bangong suture, central Tibet. Geology. 34(6):505–508. https://doi.org/10.1130/g22453.1

Haider VL, Dunkl I, von Eynatten H, Ding L, Frei D, Zhang L (2013) Cretaceous to Cenozoic evolution of the northern Lhasa Terrane and the Early Paleogene development of peneplains at Nam Co, Tibetan Plateau. J Asian Earth Sci. 70:79–98. https://doi.org/10.1016/j.jseaes.2013.03.005

Hao LL, Wang Q, Wyman DA, Ou Q, Dan W, Jiang ZQ, Wu FY, Yang JH, Long XP, Li J (2016) Underplating of basaltic magmas and crustal growth in a continental arc: Evidence from Late Mesozoic intermediate-felsic intrusive rocks in Southern Qiangtang, Central Tibet. Lithos. 245:223–242. https://doi.org/10.1016/j.lithos.2015.09.015

Harris NBW, Ronghua X, Lewis CL, Hawkesworth CJ, Yuquan Z (1988) Isotope geochemistry of the 1985 Tibet Geotraverse, Lhasa to Golmud. Philos Trans R Soc Lond Ser A, Math Phys Sci. 327(1594):26–286. https://doi.org/10.1098/rsta.1988.0129

Harris NBW, Inger S, Xu R (1990) Cretaceous plutonism in Central Tibet: an example of post-collision magmatism? J Volcanol Geoth Res. 44(1–2):21–32. https://doi.org/10.1016/0377-0273(90)90009-5

He H, Li Y, Wang C, Han Z, Ma P, Xiao S (2019) Petrogenesis and tectonic implications of Late Cretaceous highly fractionated I-type granites from the Qiangtang block, central Tibet. J Asian Earth Sci. 176:337–352. https://doi.org/10.1016/j.jseaes.2019.02.022

Hetzel R, Dunkl I, Haider V, Strobl M, von Eynatten H, Ding L, Frei D (2011) Peneplain formation in southern Tibet predates the India-Asia collision and plateau uplift. Geology. 39(10):983–986. https://doi.org/10.1130/g33617c.1

Houseman GA, Molnar P (1997) Gravitational (Rayleigh-Taylor) instability of a layer with non-linear viscosity and convective thinning of continental lithosphere. Geophys J Int. 128(1):125–150. https://doi.org/10.1111/j.1365-246x.1997.tb04075.x

Hu WL, Wang Q, Tang GJ, Zhang XZ, Qi Y, Wang J, Ma YM, Yang ZY, Sun P, Hao LL (2022) Late Early Cretaceous magmatic constraints on the timing of closure of the Bangong-Nujiang Tethyan Ocean. Central Tibet Lithos. 416:106648. https://doi.org/10.1016/j.lithos.2022.106648

Ji WQ, Wu FY, Chung SL, Li JX, Liu CZ (2009a) Zircon U-Pb geochronology and Hf isotopic constraints on petrogenesis of the Gangdese batholith, southern Tibet. Chem Geol. 262(3–4):229–245. https://doi.org/10.1016/j.chemgeo.2009.01.020

Ji C, Yan LL, Lu L, Jin X, Huang Q, Zhang KJ (2021) Anduo Late Cretaceous high-K calc-alkaline and shoshonitic volcanic rocks in central Tibet, western China: Relamination of the subducted Meso-Tethyan oceanic plateau. Lithos. 400:106345. https://doi.org/10.1016/j.lithos.2021.106345

Jiang YH, Jiang SY, Ling HF, Dai BZ (2006) Low-degree melting of a metasomatized lithospheric mantle for the origin of Cenozoic Yulong monzogranite-porphyry, east Tibet: Geochemical and Sr-Nd-Pb-Hf isotopic constraints. Earth Planet Sci Lett. 241(3–4):617–633. https://doi.org/10.1016/j.epsl.2005.11.023

Jiang YH, Liu Z, Jia RY, Liao SY, Zhou Q, Zhao P (2012) Miocene potassic granite–syenite association in western Tibetan Plateau: Implications for shoshonitic and high Ba–Sr granite genesis. Lithos. 134:146–162. https://doi.org/10.1016/j.lithos.2011.12.012

Kapp P, Yin A, Harrison TM, Ding L (2005) Cretaceous-Tertiary shortening, basin development, and volcanism in central Tibet. Geol Soc Am Bull. 117(7–8):865–878. https://doi.org/10.1130/b25595.1

Kapp P, DeCelles PG, Gehrels GE, Heizler M, Ding L (2007) Geological records of the Lhasa-Qiangtang and Indo-Asian collisions in the Nima area of central Tibet. Geol Soc Am Bull. 119(7–8):917–932. https://doi.org/10.1130/b26033.1

La Flèche MR, Camiré G, Jenner GA (1998) Geochemistry of postAcadian, Carboniferous continental intraplate basalts from the Maritimes basin, Magdalen Islands, Québec. Can Chem Geol. 148(3–4):115–136. https://doi.org/10.1016/s0009-2541(98)00002-3

Lee HY, Chung SL, Lo CH, Ji J, Lee TY, Qian Q, Zhang Q (2009) Eocene Neotethyan slab breakoff in southern Tibet inferred from the Linzizong volcanic record. Tectonophysics. 477(1–2):20–35. https://doi.org/10.1016/j.tecto.2009.02.031

Li Y, He J, Wang C, Santosh M, Dai J, Zhang Y, Wei Y, Wang J (2013) Late Cretaceous K-rich magmatism in central Tibet: Evidence for early elevation of the Tibetan plateau? Lithos. 160:1–13. https://doi.org/10.1016/j.lithos.2012.11.019

Li Y, He J, Han Z, Wang C, Ma P, Zhou A, Liu SA, Xu M (2016) Late Jurassic sodium-rich adakitic intrusive rocks in the southern Qiangtang Terrane, central Tibet, and their implications for the Bangong-Nujiang ocean subduction. Lithos. 245:34–46. https://doi.org/10.1016/j.lithos.2015.10.014

Lin IJ, Chung SL, Chu CH, Lee HY, Gallet S, Wu G, Ji J, Zhang Y (2013) Geochemical and Sr-Nd isotopic characteristics of Cretaceous to paleocene granitoids and volcanic rocks, SE Tibet: Petrogenesis and tectonic implications. J Asian Earth Sci. 53:131–150. https://doi.org/10.1016/j.jseaes.2012.03.010

Liu D, Zhao Z, Zhu DC, Niu Y, Harrison TM (2014) Zircon xenocrysts in Tibetan ultrapotassic magmas: Imaging the deep crust through time. Geology. 42(1):43–46. https://doi.org/10.1130/g34902.1

Liu D, Shi R, Ding L, Huang Q, Zhang X, Yue Y, Zhang L (2017) Zircon U-Pb age and Hf isotopic compositions of Mesozoic granitoids in southern Qiangtang, Tibet: Implications for the subduction of the Bangong-Nujiang Tethyan ocean. Gondwana Res. 41:157–172. https://doi.org/10.1016/j.gr.2015.04.007

Lu LN, Cui YB, Song L, Zhao YY, Qu XM, Wang JP (2011) Geochemical characteristics and zircon LA-ICP-MS UPb dating of

Galale sharn gold (copper) deposit, Tibet and its significance. Earth Sci Front 18:224–242 (in Chinese with English abstract)
Lu L, Zhang KJ, Jin X, Zeng L, Yan LL, Santosh M (2019) Crustal thickening of the central Tibetan plateau prior to India-Asia collision: Evidence from petrology, geochronology, geochemistry and Sr–Nd–Hf isotopes of a K-rich charnockite–granite suite in eastern Qiangtang. J Petrol. 60(4):827–854. https://doi.org/10.1093/petrology/egz017
Ludwig KR (2003) ISOPLOT 3.0: A geochronological toolkit for Microsoft Excel. Special Publication No. 4 Berkeley Geochronology Center
Ma GL, Yue YH (2010) Cretaceous volcanic rocks in northern Lhasa block: Constraints on the tectonic evolution of Gangdise arc. Acta Petrol et Mineral. 29(5):525–538 (**in Chinese with English abstract**).
Ma Y, Ruan W, Niu C, Yang T (2022) Movement history of the microcontinents from the Tibetan plateau based on paleomagnetic results with sufficient sampling units. J Earth Sci. 33(5):1072–1080. https://doi.org/10.1007/s12583-022-1721-2
Meng FY, Zhao ZD, Zhu DC, Mo XX, Guan Q, Huang Y, Dong GC, Zhou S, DePaolo DJ, Harrison TM, Zhang ZC, Liu JL, Liu YS, Hu ZC, Yuan HL (2014) Late Cretaceous magmatism in Mamba area, central Lhasa subterrane: Products of backarc extension of Neo-Tethyan Ocean? Gondwana Res. 26(2):506–520. https://doi.org/10.1016/j.gr.2013.07.017
Miller CF, Hatcher RD Jr, Mark Harrison T, Coath CD, Gorisch EB (1998) Cryptic crustal events elucidated through zone imaging and ion microprobe studies of zircon, southern Appalachian Blue Ridge. North Carolina-Georgia Geology. 26(5):419–422. https://doi.org/10.1130/0091-7613(1998)026%3c0419:cceetz%3e2.3.co;2
Mo XX, Hou Z, Niu Y, Dong G, Qu X, Zhao Z, Yang Z (2007) Mantle contributions to crustal thickening during continental collision: Evidence from Cenozoic igneous rocks in southern Tibet. Lithos. 96(1–2):225–242. https://doi.org/10.1016/j.lithos.2006.10.005
Moyen JF (2009) High Sr/Y and La/Yb ratios: The meaning of the "adakitic signature." Lithos. 112(3–4):556–574. https://doi.org/10.1016/j.lithos.2009.04.001
Moyen JF, Martin H (2012) Forty years of TTG research. Lithos. 148:312–336. https://doi.org/10.1016/j.lithos.2012.06.010
Murphy MA, Yin A, Harrison TM, Dürr S, Chen Z, Ryerson FJ, Kidd WSF, Wang X, Zhou X (1997) Did the Indo-Asian collision alone create the Tibetan Plateau? Geology. 25(8):7 19–722. https://doi.org/10.1130/0091-7613(1998)026<0958:dtiaca>2.3.co;2
Pan G, Ding J, Yao D, Wang L (2004) Guidebook of 1:1.500.000 geologic map of the Qinghai-Xizang (Tibet) plateau and adjacent areas. Chengdu Cartographic Publishing House, Chengdu, China, p 48.
Pan FB, Zhang HF, Xu WC, Guo L, Wang S, Luo B (2014) U-Pb zircon chronology, geochemical and Sr–Nd isotopic composition of Mesozoic-Cenozoic granitoids in the SE Lhasa terrane: Petrogenesis and tectonic implications. Lithos. 192:142–157. https://doi.org/10.1016/j.lithos.2014.02.005
Patiño Douce AE (1999) What do experiments tell us about the relative contributions of crust and mantle to the origin of granitic magmas? Geol Soc Lond, Spec Publ. 168(1):55–75. https://doi.org/10.1144/gsl.sp.1999.168.01.05
Patiño Douce AE, Beard JS (1995) Dehydration-melting of biotite gneiss and quartz amphibolite from 3 to 15 kbar. J Petrol. 36(3):707–738. https://doi.org/10.1093/petrology/36.3.707
Peng T, Wilde SA, Fan W, Peng B (2013) Late Neoarchean potassic high Ba–Sr granites in the Taishan granite–greenstone terrane: Petrogenesis and implications for continental crustal evolution. Chem Geol. 344:23–41. https://doi.org/10.1016/j.chemgeo.2013.02.012
Petford N, Atherton M (1996) Na-rich partial melts from newly underplated basaltic crust: The cordillera blanca batholith. Peru J Petrol. 37(6):1491–1521. https://doi.org/10.1093/petrology/37.6.1491
Petford N, Gallagher K (2001) Partial melting of mafic (amphibolitic) lower crust by periodic influx of basaltic magma. Earth Planet Sci Lett. 93(3–4):483–499. https://doi.org/10.1016/s0012-821x(01)00481-2
Plank T (2014) 4.17 - The chemical composition of subducting sediments. In: Holland HD, Turekian KK (eds) Treatise on geochemistry, 2nd edn. Elsevier, Oxford, pp 607–629. https://doi.org/10.1016/b978-0-08-095975-7.00319-3
Polat A, Kerrich R (2001) Magnesian andesites, Nb-enriched basalt-andesites, and adakites from Late-Archean 2.7 Ga Wawa greenstone belts, Superior province, Canada: Implications for Late Archean subduction zone petrogenetic processes. Contrib Mineral Petrol. 141(1):36–52. https://doi.org/10.1007/s004100000223
Qi L, Hu J, Gregoire DC (2000) Determination of trace elements in granites by inductively coupled plasma mass spectrometry. Talanta. 51(3):507–513. https://doi.org/10.1016/s0039-9140(99)00318-5
Qian Q, Chung SL, Li TY, Wen DR (2002) Geochemical characteristics and petrogenesis of the Badaling high Ba–Sr granitoids: a comparison of igneous rocks from North China and the Dabie-Sulu Orogen. Acta Pet Sin. 18:275–292 (**in Chinese with English abstract**)
Qu XM, Xin HB (2006) Age and tectonic environment of the Bangong Co porphyry copper belt in western Tibet. China Geol Bull. 25:792–799 (**in Chinese with English abstract**).
Qu XM, Wang RJ, Xin HB, Jiang JH, Chen H (2012) Age and petrogenesis of A-type granites in the middle segment of the Bangonghu-Nujiang suture, Tibetan Plateau. Lithos. 146:264–275. https://doi.org/10.1016/j.lithos.2012.05.006
Rapp RP, Watson EB (1995) Dehydration melting of metabasalt at 8–32 kbar: Implications for continental growth and crust-mantle recycling. J Petrol. 36(4):891–931. https://doi.org/10.1093/petrology/36.4.891
Rapp RP, Shimizu N, Norman MD, Applegate GS (1999) Reaction between slab-derived melts and peridotite in the mantle wedge: experimental constraints at 3.8 GPa. Chem Geol. 160(4):335–356. https://doi.org/10.1016/s0009-2541(99)00106-0
Rapp B, Perrotin F, Marret H, Sembely-Taveau C, Lansac J, Body G (2002) Value of fetal cerebral magnetic resonance imaging for the prenatal diagnosis and prognosis of corpus callosum agenesis. J Gynecol Obstet Biol Reprod 31(2 Pt 1):173–182.
Rudnick RL, Fountain DM (1995) Nature and composition of the continental crust: A lower crustal perspective. Rev Geophys. 33(3):267–309. https://doi.org/10.1029/95rg01302
Rudnick RL, Gao S (2014) 4.1 - Composition of the continental crust. In: Holland HD, Turekian KK (eds) Treatise on geochemistry, 2nd edn. Elsevier, Oxford, pp 1–51.
Rudnick RL, Mcdonough WF, Chappell BW (1993) Carbonatite metasomatism in the northern Tanzanian mantle: Petrographic and geochemical characteristics. Earth Planet Sci Lett. 114(4):463–475. https://doi.org/10.1016/0012-821x(93)90076-l
Sui QL, Wang Q, Zhu DC, Zhao ZD, Chen Y, Santosh M, Hu ZC, Yuan HL, Mo XX (2013) Compositional diversity of ca. 110 Ma magmatism in the northern Lhasa Terrane, Tibet: Implications for the magmatic origin and crustal growth in a continent–continent collision zone. Lithos. 168:144–159. https://doi.org/10.1016/j.lithos.2013.01.012
Sun SS, McDonough WF (1989) Chemical and isotopic systematics of oceanic basalts: Implications for mantle composition and

processes. Geol Soc Lond, Spec Publ. 42(1):313–345. https://doi.org/10.1144/gsl.sp.1989.042.01.19

Sun GY, Hu XM, Zhu DC, Hong WT, Wang JG, Wang Q (2015a) Thickened juvenile lower crust-derived ~90 Ma adakitic rocks in the central Lhasa terrane. Tibet Lithos. 224:225–239. https://doi.org/10.1016/j.lithos.2015.03.010

Sun GY, Hu XM, Sinclair HD, BouDagher-Fadel MK, Wang JG (2015b) Late Cretaceous evolution of the Coqen basin (Lhasa terrane) and implications for early topographic growth on the Tibetan Plateau. GSA Bull. 127(7–8):1001–1020. https://doi.org/10.1130/b31137.1

Sun M, Tang JX, Chen W, Ma XD, Qu XM, Song Y, Li XY, Ding JS (2020) Process of lithospheric delamination beneath the Lhasa-Qiangtang collision orogen: Constraints from the geochronology and geochemistry of Late Cretaceous volcanic rocks in the Lhasa terrane, central Tibet. Lithos. 356:105219. https://doi.org/10.1016/j.lithos.2019.105219

Sun P, Wang Q, Hao LL, Dan W, Ou Q, Jiang ZQ, Tang GJ (2021) A mélange contribution to arc magmas recorded by Nd-Hf isotopic decoupling: An example from southern Qiangtang block, Central Tibet. J Asian Earth Sci. 221:1367–9120. https://doi.org/10.1016/j.jseaes.2021.104931

Tang M, Wang XL, Shu XJ, Wang D, Yang T, Gopon P (2014) Hafnium isotopic heterogeneity in zircons from granitic rocks: Geochemical evaluation and modeling of "zircon effect" in crustal anatexis. Earth Planet Sci Lett. 389:188–199. https://doi.org/10.1016/j.epsl.2013.12.036

Tang GJ, Wang Q, Wyma DA, Dan W (2019) Crustal maturation through chemical weathering and crustal recycling revealed by Hf–O–B isotopes. Earth Planet Sci Lett 524: https://doi.org/10.1016/j.epsl.2019.115709

Tarney J, Jones CE (1994) Trace element geochemistry of orogenic igneous rocks and crustal growth models. J Geol Soc Lond. 151(5):855–868. https://doi.org/10.1144/gsjgs.151.5.0855

Vervoort JD, Plank T, Prytulak J (2011) The Hf–Nd isotopic composition of marine sediments. Geochim Cosmochim Acta. 75(20):5903–5926. https://doi.org/10.1016/j.gca.2011.07.046

Wang BD, Xu JF, Liu BM, Chen JL, Wang LQ, Guo L, Wang DB, Zhang WP (2013) Geochronology and ore–forming geological background of 90 Ma porphyry copper deposit in the Lhasa terrane. Tibet plateau. Acta Geol Sin 87(1):71–80 (in Chinese with English abstract)

Wang Q, Zhu DC, Zhao ZD, Liu SA, Chung SL, Li SM, Liu D, Dai JG, Wang LQ, Mo XX (2014) Origin of the ca. 90 Ma magnesia-rich volcanic rocks in Se Nyima, central Tibet: Products of lithospheric delamination beneath the Lhasa-qiangtang collision zone. Lithos. 198:24–37. https://doi.org/10.1016/j.lithos.2014.03.019

Wang XS, Williams-Jones AE, Bi XW, Hu RZ, Xiao JF, Huang ML (2019) Late Cretaceous Transtension in the Eastern Tibetan Plateau: evidence from postcollisional A-type granite and syenite in the Changdu area, China. J Geophy Res: Solid Earth. 124(7):6409–6427. https://doi.org/10.1029/2018jb017072

Wang ZL, Fan JJ, Wang Q, Hu WL, Yang ZY, Wang J (2021) Reworking of juvenile crust beneath the Bangong-Nujiang suture zone: evidence from Late Cretaceous granite porphyries in Southern Qiangtang. Cent Tibet Lithos. 390:106097. https://doi.org/10.1016/j.lithos.2021.106097

Wang X, Sun M, Weinberg RF, Cai K, Zhao G, Xia X, Li P, Liu X (2022a) Adakite generation as a result of fluid-fluxed melting at normal lower crustal pressures. Earth Planet Sci Lett. 594:117744. https://doi.org/10.1016/j.epsl.2022.117744

Wang Y, Zeng L, Hou K, Gao LE, Wang Q, Zhao L, Jiahao G, Li G (2022b) Mantle source components and magmatic evolution for the comei large Igneous province: Evidence from the Early Cretaceous Niangzhong mafic magmatism in Tethyan Himalaya. J Earth Sci. 33(1):133–149. https://doi.org/10.1007/s12583-021-1464-5

Wang ZZ, Zhao ZD, Li XP, Liu D, Mo XX, Zhu DC, Meng YK, Tang Y, Cong FY (2023) The process of crustal thickening in the southern Lhasa terrane during India-Eurasia collision: Constraint from Eocene high Sr/Y rocks in the Quxu pluton. Geol Soc Am Bull. https://doi.org/10.1130/gsab.s.23460170

Wen DR, Liu D, Chung SL, Chu MF, Ji J, Zhang Q, Song B, Lee TY, Yeh MW, Lo CH (2008a) Zircon SHRIMP U-Pb ages of the Gangdese Batholith and implications for Neotethyan subduction in southern Tibet. Chem Geol. 252(3–4):191–201. https://doi.org/10.1016/j.chemgeo.2008.03.003

Wen DR, Chung SL, Song B, Iizuka Y, Yang HJ, Ji J, Liu D, Gallet S (2008b) Late Cretaceous Gangdese intrusions of adakitic geochemical characteristics, SE Tibet: Petrogenesis and tectonic implications. Lithos. 105(1–2):1–11. https://doi.org/10.1016/j.lithos.2008.02.005

Wen DJ, Hu X, Chapman T, Zeng G, Ma AL, Wang RQ (2023) Late Cretaceous bimodal volcanic rocks in Shuanghu induced by lithospheric delamination beneath the Southern Qiangtang. Tibet Lithos. 460:107368. https://doi.org/10.1016/j.lithos.2023.107368

Workman RK, Hart SR (2005) Major and trace element composition of the depleted MORB mantle (DMM). Earth Planet Sci Lett. 231(1–2):53–72. https://doi.org/10.1016/j.epsl.2004.12.005

Xu RH, Scharer U, Allègre CJ (1985) Magmatism and metamorphism in the Lhasa block (Tibet): A geochronological study. J Geol. 93(1):41–57. https://doi.org/10.1086/628918

Yao XF, Tang JX, Li ZJ, Deng SL, Ding S, Hu ZH, Zhang Z (2013) The redefinition of the ore-forming porphyry's age in Gaerqiong skarn-type gold-copper deposit, western Bangong Lake-Nujiang River metallogenic belt, Xizang (Tibet). Geol Rev 59:193–200 (in Chinese with English abstract)

Ye HM, Li XH, Li ZX, Zhang CL (2008) Age and origin of high Ba–Sr appinite–granites at the northwestern margin of the Tibet Plateau: Implications for Early Paleozoic tectonic evolution of the western Kunlun orogenic belt. Gondwana Res. 13(1):126–138. https://doi.org/10.1016/j.gr.2007.08.005

Yi JK, Wang Q, Zhu DC, Li SM, Liu SA, Wang R, Zhang LL, Zhao ZD (2018) Westward-younging high-Mg adakitic magmatism in central Tibet: Record of a westward-migrating lithospheric foundering beneath the Lhasa-Qiangtang collision zone during the Late Cretaceous. Lithos. 316:92–103. https://doi.org/10.1016/j.lithos.2018.07.001

Yin A, Harrison TM (2000) Geologic evolution of the Himalayan-Tibetan orogen. Annu Rev Earth Planet Sci. 28(1):211–280. https://doi.org/10.1146/annurev.earth.28.1.211

Yu HX, Chen JL, Xu JF, Wang BD, Wu JB, Liang YH (2011) Geochemistry and origin of Late Cretaceous (~90 Ma) mineral porphyry of Balazha in mid-northern Lhasa terrane. Tibet Acta Petrol Sin. 27(07):2011–2022 (**in Chinese with English abstract**).

Yu YS, Yang ZS, Dai PY, Tian SH, Gao Y, Liu YC, Xiu D (2015) Geochronology and genesis of the magmatism in the Ria copper polymetallic deposit of the Nixiong orefield, Coqen. Tibet. Geol China 42:118–133 (in Chinese with an English abstract)

Yuan HL, Gao S, Liu XM, Li HM, Gunther D, Wu FY (2004) Accurate U-Pb age and trace element determinations of zircon by laser ablation-inductively coupled plasma mass spectrometry. Geo-Stand Newslett. 28(3):353–370. https://doi.org/10.1111/j.1751-908x.2004.tb00755.x

Yuan HL, Gao S, Dai MN, Zong CL, Gunther D, Fontaine GH, Liu XM, Diwu CR (2008) Simultaneous determinations of U-Pb age, Hf isotopes and trace element compositions of zircon by excimer laser-ablation quadrupole and multiple-collector ICP-MS. Chem Geol. 247(1–2):100–118. https://doi.org/10.1016/j.chemgeo.2007.10.003

Zhang KJ (2004) Secular geochemical variations of the Lower Cretaceous siliciclastic rocks from central Tibet (China) indicate a tectonic transition from continental collision to back-arc rifting. Earth Planet Sci Lett. 229(1–2):73–89. https://doi.org/10.1016/j.epsl.2004.10.030

Zhang Z, Ding L, Zhao Z, Santosh M (2017) Tectonic evolution and dynamics of the Tibetan Plateau. Gondwana Res. 41:1–8. https://doi.org/10.1016/j.gr.2016.09.001

Zhao TP, Zhou MF, Zhao JH, Zhang KJ, Chen W, Zhou M, Zhao J, Zhang K, Chen AW (2008) Geochronology and geochemistry of the ca. 80 Ma Rutog granitic pluton, northwestern Tibet: Implications for the tectonic evolution of the Lhasa terrane. Geol Mag. 145(6):845–857. https://doi.org/10.1017/s0016756808005025

Zheng YF, Wu RX, Wu YB, Zhang SB, Yuan HL, Wu FY (2008) Rift melting of juvenile arc-derived crust: Geochemical evidence from Neoproterozoic volcanic and granitic rocks in the Jiangnan Orogen, South China. Precambrian Res. 136(3–4):351–383. https://doi.org/10.1016/j.precamres.2008.01.004

Zhu DC, Mo XX, Wang LQ, Zhao ZD, Niu YL, Zhou CY, Yang YH (2009a) Petrogenesis of highly fractionated I-type granites in the Zayu area of eastern Gangdese, Tibet: Constraints from zircon U-Pb geochronology, geochemistry and Sr-Nd-Hf isotopes. Sci China Ser D: Earth Sci. 52(9):1223–1239. https://doi.org/10.1007/s11430-009-0132-x

Zhu DC, Mo XX, Niu YL, Zhao ZD, Wang LQ, Liu YS, Wu FY (2009b) Geochemical investigation of Early Cretaceous igneous rocks along an east-west traverse throughout the central Lhasa Terrane, Tibet. Chem Geol. 268(3–4):298–312. https://doi.org/10.1016/j.chemgeo.2009.09.008

Zhu DC, Zhao ZD, Niu Y, Mo XX, Chung SL, Hou ZQ (2011) The Lhasa Terrane: Record of a microcontinent and its histories of drift and growth. Earth Planet Sci Lett. 301(1–2):241–255. https://doi.org/10.1016/j.epsl.2010.11.005

Zhu DC, Zhao ZD, Niu YL, Dilek Y, Hou ZQ, Mo XX (2013) The origin and pre-Cenozoic evolution of the Tibetan Plateau. Gondwana Res. 23(1–2):1429–1454. https://doi.org/10.1016/j.epsl.2010.11.005

Zhu DC, Li SM, Cawood PA, Wang Q, Zhao ZD, Liu SA, Wang LQ (2015) Assembly of the Lhasa and Qiangtang terranes in central Tibet by divergent double subduction. Lithos. 245(1–2):7–17. https://doi.org/10.1016/j.lithos.2015.06.023

Zhu RZ, Lai SC, Fowler M, Xie JC, Glynn SM (2023) A microcosm of modern crust formation: Evidence from zircon ages, Hf O and Nd Sr isotopes and bulk geochemistry of the Menglian Batholith, SE Tibet. Chem Geol. 618:121276. https://doi.org/10.1016/j.chemgeo.2022.121276

Zhu RZ, Smith DJ, Wang F, Qin JF, Zhang C, Zhao SW, Liu M, Zhang FY, Zhu Y, Lai SC (2024) Hornblendites as a record of differentiation, metasomatism and magma fertility in arc crust. Chem Geol. https://doi.org/10.1016/j.chemgeo.2024.121974